

The evolution of the cluster X-ray scaling relations in the WARPS sample at $0.6 < z < 1.0$.

B. J. Maughan,^{1,2*}† L. R. Jones,¹ H. Ebeling,³ and C. Scharf⁴

¹*School of Physics and Astronomy, The University of Birmingham, Edgbaston, Birmingham B15 2TT, UK.*

²*Harvard-Smithsonian Center for Astrophysics, 60 Garden St, Cambridge, MA 02140, USA.*

³*Institute for Astronomy, 2680 Woodlawn Drive, Honolulu, HI 96822, USA.*

⁴*Columbia Astrophysics Laboratory, MC 5247, 550 West 120th St., New York, NY 10027, USA.*

arXiv:astro-ph/0503455v2 14 Oct 2005

29 July 2018

ABSTRACT

The X-ray properties of a sample of 11 high-redshift ($0.6 < z < 1.0$) clusters observed with *Chandra* and/or *XMM-Newton* are used to investigate the evolution of the cluster scaling relations. The observed evolution in the normalisation of the $L - T$, $M - T$, $M_g - T$, and $M - L$ relations are consistent with simple self-similar predictions, in which the properties of clusters reflect the properties of the universe at their redshift of observation. Under the assumption that the model of self-similar evolution is correct and that the local systems formed via a single spherical collapse, the high-redshift $L - T$ relation is consistent with the high- z clusters having virialised at a significantly higher redshift than the local systems. The data are also consistent with the more realistic scenario of clusters forming via the continuous accretion of material.

The slope of the $L - T$ relation at high-redshift ($B = 3.32 \pm 0.37$) is consistent with the local relation, and significantly steeper than the self-similar prediction of $B = 2$. This suggests that the same non-gravitational processes are responsible for steepening the local and high- z relations, possibly occurring universally at $z \gtrsim 1$ or in the early stages of the clusters' formation, prior to their observation.

The properties of the intra-cluster medium at high-redshift are found to be similar to those in the local universe. The mean surface-brightness profile slope for the sample is $\beta = 0.66 \pm 0.05$, the mean gas mass fractions within $R_{2500(z)}$ and $R_{200(z)}$ are 0.069 ± 0.012 and 0.11 ± 0.02 respectively, and the mean metallicity of the sample is $0.28 \pm 0.11 Z_{\odot}$.

Key words: cosmology: observations – galaxies: clusters: general – galaxies: high-redshift – intergalactic medium – X-rays: galaxies

1 INTRODUCTION

A simple and useful model to describe galaxy clusters is that they are self-similar. In this model, clusters form via the collapse of the most overdense regions in the early universe, and the cluster baryons are heated only by gravitational processes (compression and shock heating) during the collapse. The properties of clusters at high redshift are then identical to those of their low-redshift counterparts, apart from scaling factors reflecting the increase of the mean density of the universe with redshift. This scaling with redshift has been termed weak self-similarity (*e.g.* Bower 1997). In the strongest form of the model, the mass profiles of all clusters

at the same epoch follow the same shape independent of their total mass. The self-similar model then allows properties of clusters of different masses and at different redshifts to be related to one-another according to simple scaling laws.

X-ray observations provide a powerful way of measuring cluster properties, and have provided a wealth of evidence that galaxy clusters do not scale self-similarly with mass (or, by proxy, temperature) in the local universe. For example; the slope of the X-ray luminosity-temperature ($L - T$) relation is steeper than self-similar predictions (*e.g.* Markevitch 1998; Arnaud & Evrard 1999); the slopes of the gas-density and surface-brightness profiles are shallower in cooler systems (*e.g.* Lloyd-Davies et al. 2000; Sanderson et al. 2003); and the entropy in cluster cores is higher than predicted (*e.g.* Ponman et al. 1999, 2003). These departures from self-similarity are generally taken as evidence for the importance

* E-mail: bmaughan@cfa.harvard.edu

† Chandra Fellow

of non-gravitational contributions (such as heating by AGN or radiative cooling) to the energy budget of clusters.

In this paper we address the open question of whether the simple evolution of the cluster scaling relations predicted by the self-similar model is obeyed. We define evolution as any change with respect to the local scaling relations, and compare any such evolution with the self-similar predictions. The results of early studies of the evolution of the L – T relation were consistent with little or no evolution (e.g. Mushotzky & Scharf 1997; Donahue et al. 1999; Fairley et al. 2000). More recent studies with *Chandra* and *XMM-Newton* have found significant evolution in the L – T relation (Vikhlinin et al. 2002; Ettori et al. 2004; Lumb et al. 2004). This change is due to the availability of larger samples of clusters at higher redshifts, and differences in the assumed cosmological model. The measured evolution is larger in a Λ CDM cosmology than in the Einstein de-Sitter models which were assumed in many of the earlier studies (e.g. Arnaud et al. 2002; Lumb et al. 2004).

Here we present an analysis of a sample of 11 clusters in the redshift range $0.6 < z \leq 1.0$ drawn from the Wide Angle *ROSAT* Pointed Survey (WARPS; Scharf et al. 1997; Perlman et al. 2002). A statistically complete, flux-limited ($F_X(0.5 - 2 \text{ keV}) > 6.4 \times 10^{-13} \text{ erg s}^{-1} \text{ cm}^{-2}$) sample of 13 WARPS clusters was originally observed with *Chandra* and/or *XMM-Newton*, but two of the *XMM-Newton* observations were rendered unusable due to extremely high background levels, leaving the 11 clusters discussed here. Of these clusters, two now fall below the flux limit due to point source contamination in the original *ROSAT* observations, however the set of 11 clusters used in this work should be fairly unbiased. These clusters' properties, and the scaling relations derived from them, are compared to those of other samples at high and low redshift, and with the predictions of different cluster-formation models.

A Λ CDM cosmology of $H_0 = 70 \text{ km s}^{-1} \text{ Mpc}^{-1} \equiv 100h_{70} \text{ km s}^{-1} \text{ Mpc}^{-1}$, and $\Omega_M = 0.3$ ($\Omega_\Lambda = 0.7$) is adopted throughout, with the convention that Ω_M represents the present-day matter density, while $\Omega_m(z)$ represents its value at redshift z . All errors are quoted at the 68% level.

2 DATA ANALYSIS

The standard data reduction steps were followed for both the *Chandra* and *XMM-Newton* observations, and are discussed in detail in Maughan et al. (2003) (*Chandra*) and Maughan et al. (2004) (*XMM-Newton*). Data reduction was performed with Ciao 3.2.2 and SAS 6.1 for *Chandra* and *XMM-Newton* respectively. In summary, the data were filtered to remove high-background periods, and a surface-brightness profile was extracted (with point sources excluded) to determine the extent of the cluster emission. The detection radius (r_d) of the cluster was then defined as the radius outside which no further emission was detected at the 3σ level in the surface-brightness profile. Spectra were extracted from within the detection radius, and were fit in the $0.4 - 7 \text{ keV}$ band with an absorbed MEKAL model (Kaastra & Mewe 1993). The low energy cutoff was chosen to minimise calibration uncertainties at low energies for both *XMM-Newton* and *Chandra*. Ignoring energies above 7 keV has little effect on *Chandra* data due to the low effective area at those energies, and

avoids instrumental fluorescent lines at $\sim 8 \text{ keV}$ which vary spatially across the *XMM-Newton* PN detector. The absorbing column was frozen at the Galactic value determined from 21 cm radio observations (Dickey & Lockman 1990) during the spectral fits. When the spectra were of sufficient quality, the absorbing column was also fit, and found to be consistent with the Galactic value. The surface-brightness distribution of each system was modeled with a two-dimensional β -model (Cavaliere & Fusco-Femiano 1976).

The issue of background subtraction was carefully considered when modeling both the spectra and the surface-brightness distributions. In all cases the background was measured from the same observation in a region as close to the source as possible, while avoiding contaminating source emission. Due to the higher background levels in the *XMM-Newton* observations, the background in the *XMM-Newton* surface-brightness models included two components to account for the flat and vigneted background components (Maughan et al. 2004). Consistency checks were performed for several clusters from the sample using backgrounds derived from different regions of the source datasets and from blank-sky datasets (e.g. Maughan et al. 2003; Maughan et al. 2004). The derived properties were generally independent of the background used. Point sources were masked out from all source and background regions during the analyses.

During the spectral-fitting process, the model redshifts were frozen at the values derived from optical spectroscopy, and best-fitting temperatures were found with the metallicity (Z) fixed at $0.3Z_\odot$. The metallicity parameter was then allowed to vary in addition to the model temperature and normalisation, and its best-fitting value was found. In all cases, the best-fitting model temperatures obtained with and without the metallicity free to vary agreed within 1σ . As the metallicities were not always well constrained, the temperatures derived with metallicity fixed at $0.3Z_\odot$ are used throughout this work. The effective area of the instruments was taken into account in the spectral modeling by using ancillary response files (ARFs) generated for the cluster positions, and weighted by the spatial distributions of source photons.

For the purposes of spectral fitting, additional filtering was applied to the *XMM-Newton* data retaining only events with FLAG and PATTERN parameters equal to zero. These correspond to events detected in single pixels which were not close to CCD gaps. The energy calibration of these events is the most reliable. The loss of effective area to CCD gaps, bad pixels, and excluded point sources within the spectral extraction region was accounted for by correcting the normalisation of the ARFs. While the ARF files already account for these losses in principal, they do not take into account the surface brightness distribution of the source. We included this effect in our correction as follows. For each cluster, a background-subtracted radial profile of the source region was produced, excluding "dead regions" (CCD gaps, bad pixels and point sources). In each radial bin, the measured flux was used to predict the number of counts that would have been detected if there were no dead regions. These counts were summed over the source region, and the ARF normalisation was scaled by the ratio of the detected counts to the predicted total counts if there were no dead regions. This process was not required for the *Chandra* observations as the spectral extraction regions were unaffected by dead

regions. The spectral redistribution matrix files were generated with SAS version 6.1 using the calibration database appropriate for that release, which included improved calibration of the PN response at low energies.

All of the clusters in our sample, with the exception of ClJ0046.3+8530, were the target of their observations and were located close to the optical axis. However ClJ0046.3+8530 was observed serendipitously near the edge of the field of view in two *XMM-Newton* observations, which introduced some additional calibration issues due to the broader PSF. The analysis of this system is discussed in detail in Maughan et al. (2004).

The slope (β) and core radius (r_c) of the gas-density profile were derived from a two-dimensional elliptical β -model fitted to an image of the cluster emission, including the effects of vignetting and the PSF. The ellipticity of the model was defined as $e = (1 - b/a)$, where a and b are the semi-major and -minor axes respectively. With the central gas density derived from the normalisation of the best-fitting spectral model (e.g. Maughan et al. 2003), it was then possible to derive the gas-mass profile assuming spherical symmetry. The total mass profile was then derived under the assumptions of isothermality, hydrostatic equilibrium, and spherical symmetry. From this total mass profile, an over-density profile (with respect to the critical density $\rho_c(z)$ at the cluster's redshift) was derived, enabling the measurement of over-density radii, R_Δ . Here R_Δ refers to the radius within which the mean density is $\Delta\rho_c(z)$, and Δ is an over-density factor. We take Δ to be a function of redshift, as explained in §4, and denote radii defined in this way as e.g. $R_{200(z)}$ where $\Delta = 200$ at $z = 0$.

2.1 Computation of errors

The uncertainties on the derived properties of a cluster were obtained in the following way. Distributions of the derived properties were computed from 10,000 randomisations of the observed properties within their uncertainty distributions. The 1σ confidence limits on each of the derived properties were then obtained from the ± 34 percentiles about the best-fit value. This method treats the statistical uncertainties in extrapolating properties to different radii self-consistently, but does not account for any systematic uncertainties in extrapolating properties beyond the limits of the data. A significant source of systematic uncertainty is the assumption of isothermality. Data of sufficient quality to measure temperature profiles were only available for two clusters in the sample, and in those cases the assumption of isothermality was justified. The systematic effect that undetected temperature gradients could have on derived masses is discussed in §7 and §8.

An additional consideration is the well known positive correlation between the β and r_c surface-brightness profile parameters. Models with large β and r_c are similar to those with small values of the parameters. The error treatment described above assumes that all errors are independent. The effect of this assumption was investigated in the following way: A simple cluster image was simulated by adding Poisson noise to a two-dimensional β -profile image. A β -model was then fit to this image, and a two-dimensional probability distribution of β and r_c values was generated. Cluster properties were then derived for an assumed tem-

perature and MEKAL normalisation, and the uncertainties were computed by sampling pairs of β and r_c values from the two-dimensional probability distribution, thereby accurately reflecting their correlated errors. The uncertainties on all other parameters were assumed to be negligible. This process was repeated assuming uncorrelated β and r_c errors, and also assuming negligible errors on r_c . It was found that the latter two methods gave similar uncertainties on cluster properties, and these uncertainties were approximately twice as large as those derived using the true, correlated errors on β and r_c . In fact, the uncertainties on the properties of the observed clusters are dominated by the measurement errors on the temperature, and the choice between these methods makes a negligible contribution to the error budget. With this in mind, the measurement errors on r_c were ignored in the calculation of the errors on all cluster properties.

An interesting consequence of this self-consistent treatment of errors is that the fractional uncertainty on R_{2500} is in general significantly larger than that on R_{200} . This is in spite of the fact that the data for all of the clusters extend beyond R_{2500} , but must be extrapolated to R_{200} (see Table 1). The reason for this is that without including any systematic uncertainties due to the extrapolation, the distribution of β values has a larger effect on the shape of the density profile at small radii than large ($>> r_c$) radii. Fig. 1 illustrates this point, showing a range of 50 over-density profiles derived for a 5.5 keV cluster at $z = 0.833$ with $r_c = 250$ kpc and values of β randomly drawn from the distribution 0.67 ± 0.07 . These uncertainties on β are the average fractional uncertainties on our sample, and so reflect the typical uncertainty in the shape of the over-density profiles. In these simulations, the fractional error on R_{2500} is 0.11, while that on R_{200} is 0.05. The self-consistent treatment of the uncertainties can thus result in larger fractional error on quantities derived within the extent of the data than those extrapolated to large radii beyond the data. While the measurement errors on kT have a large effect on the uncertainty in the normalisation of the over-density profiles, this source of uncertainty is not important for this comparison as it does not affect the shape of the profiles.

3 THE SAMPLE

In this section each cluster in the sample is discussed briefly, highlighting any unusual or interesting aspects of its analysis and properties. Images of each of the clusters with contours of the adaptively smoothed X-ray emission overlaid are shown in Fig. 2 and the observed properties of the sample are summarised in Table 1 in redshift order. The detection radii of each cluster as a fraction of $R_{2500(z)}$ and $R_{200(z)}$ are also given in Table 1. The method used to define and measure these over-density radii is described in §4 and their values are given in Table 2 for each cluster.

ClJ0046.3+8530. This cluster was observed serendipitously 11' off axis in two consecutive *XMM-Newton* observations of the open star cluster NGC 188. These data are discussed in detail in Maughan et al. (2004). The cluster has a reasonably relaxed morphology, and its temperature profile and hardness-ratio map are consistent with isothermality out to 70% of the virial radius, within the statistical limits of the data.

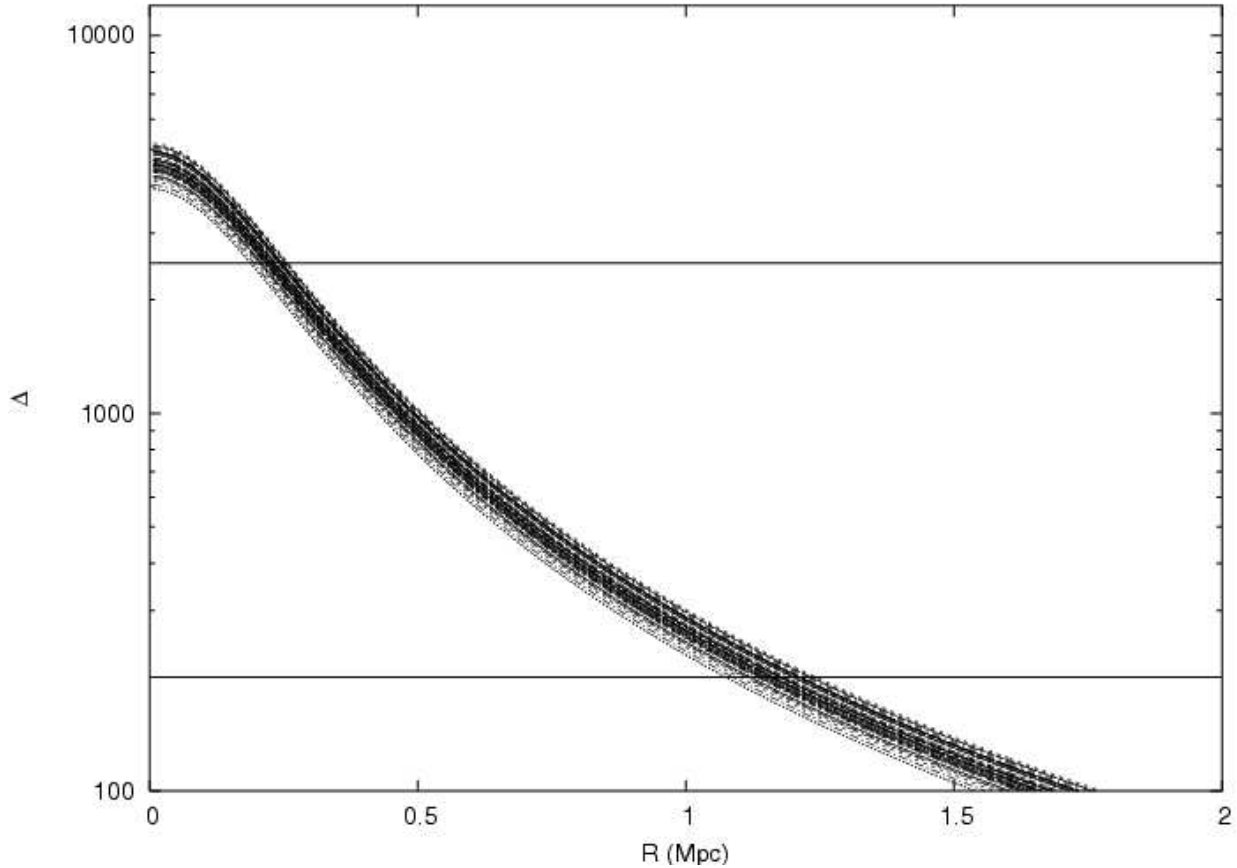


Figure 1. 50 sample overdensity profiles generated for a distribution of β values. The horizontal lines mark overdensities of 200 and 2500. The overdensity at R is defined as the ratio of the mean density within R to the critical density.

ClJ1342.9+2828. The *XMM-Newton* observation of this system shows a core region that is elongated in the East-West direction, with two possible X-ray peaks. This morphology is indicative of a late-stage merger.

ClJ1113.1–2615. The *Chandra* observation of this cluster, which is discussed in detail in Maughan et al. (2003), shows a reasonably relaxed, although slightly elliptical, morphology.

ClJ1103.6+3555. Observed with *XMM-Newton*, this cluster has a fairly disturbed X-ray morphology, suggesting that it may not have dynamically relaxed after a recent merger. It also appears to be surrounded by more extended low surface-brightness emission.

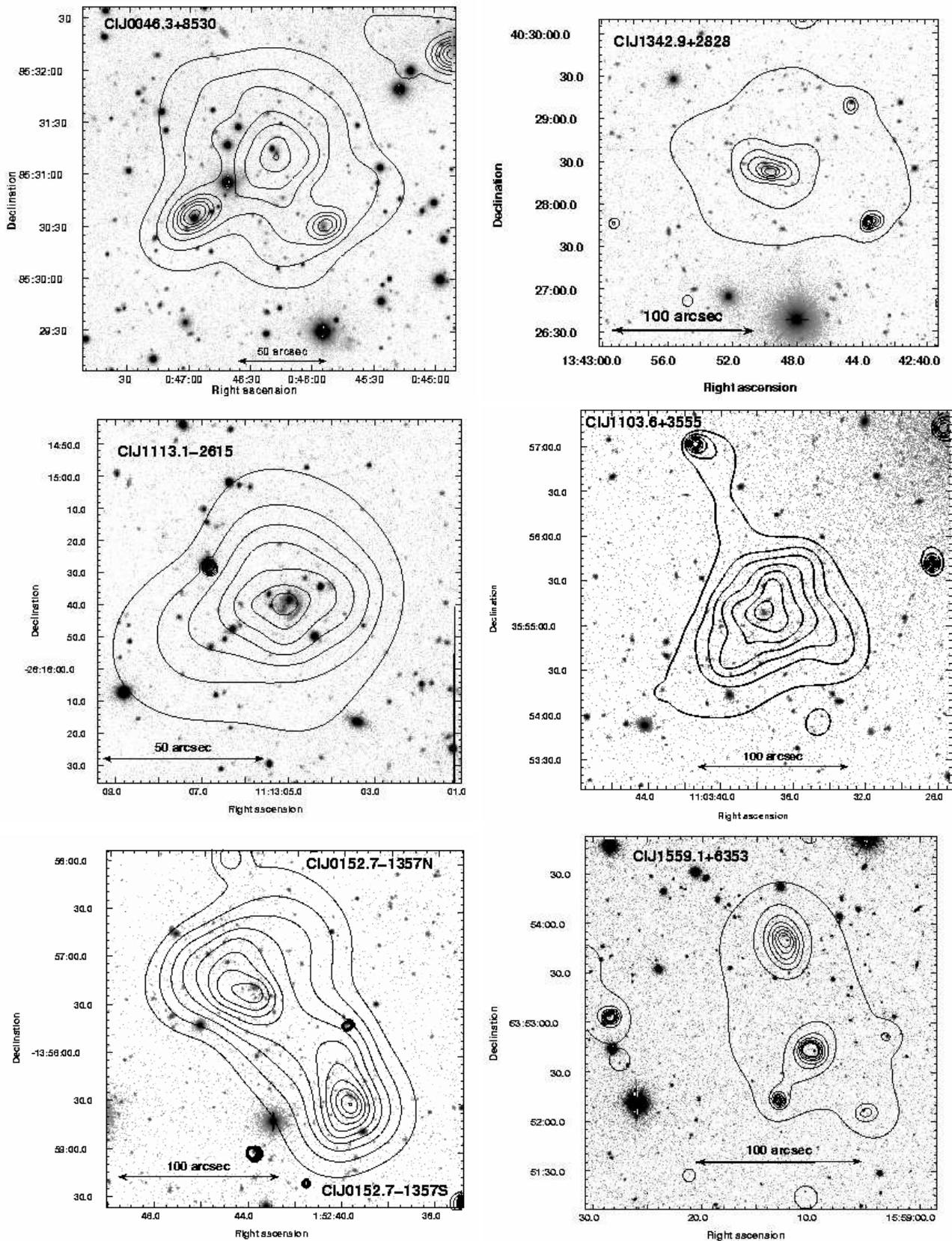
ClJ0152.7–1357. This spectacular system is probably an early-stage merger between two equally massive clusters ClJ0152.7–1357N and ClJ0152.7–1357S and has been studied in some detail (Ebeling et al. 2000; Maughan et al. 2003; Huo et al. 2004; Jee et al. 2005). The *Chandra* observation used here suggests that both of the clusters are reasonably relaxed, with ClJ0152.7–1357N the more elliptical. A recent, deep *XMM-Newton* observation has detected some substructure in ClJ0152.7–1357N, while ClJ0152.7–1357S still appears relaxed (Maughan et al. in preparation).

ClJ1559.1+6353. This cluster was observed by *XMM-Newton*. The data show an elliptical morphology ($e = 0.35$; see Table 1), suggesting that the system may not yet have fully relaxed back into hydrostatic equilibrium after its last merger event. A bright, variable point-source $\approx 1'$ South of

the cluster centroid led to an overestimate of its *ROSAT* flux in the WARPS (Horner et al. in preparation). For this system, a very high, poorly constrained metallicity was measured, with relatively poor constraints on temperature (see Table 1). This is likely to be due to some remaining contamination from the bright source caused by the large wings of the *XMM-Newton* point spread function, and to the fact that the spectrum had a lower signal-to-noise than most of the other systems discussed here.

ClJ1008.7+5342. The morphology of this cluster appears fairly relaxed in the *XMM-Newton* observation. However, the ellipticity of the best-fitting surface-brightness model is 0.27, indicating that the system may be disturbed to some degree.

ClJ1226.9+3332. This system has been the target of both *Chandra* (Cagnoni et al. 2001) and *XMM-Newton* (Maughan et al. 2004) observations, and was found to be extremely hot, with a regular, relaxed morphology. Based on a 16 ks *XMM-Newton* observation Maughan et al. (2004) measured a temperature profile and hardness-ratio map which were consistent with the cluster being isothermal out to 45% of the virial radius. In addition, the temperature and luminosity measured from the *Chandra* and *XMM-Newton* data were found to be in good agreement (Maughan et al. 2004). The properties derived from the *XMM-Newton* data are used throughout this work. A forthcoming deep *XMM-Newton*



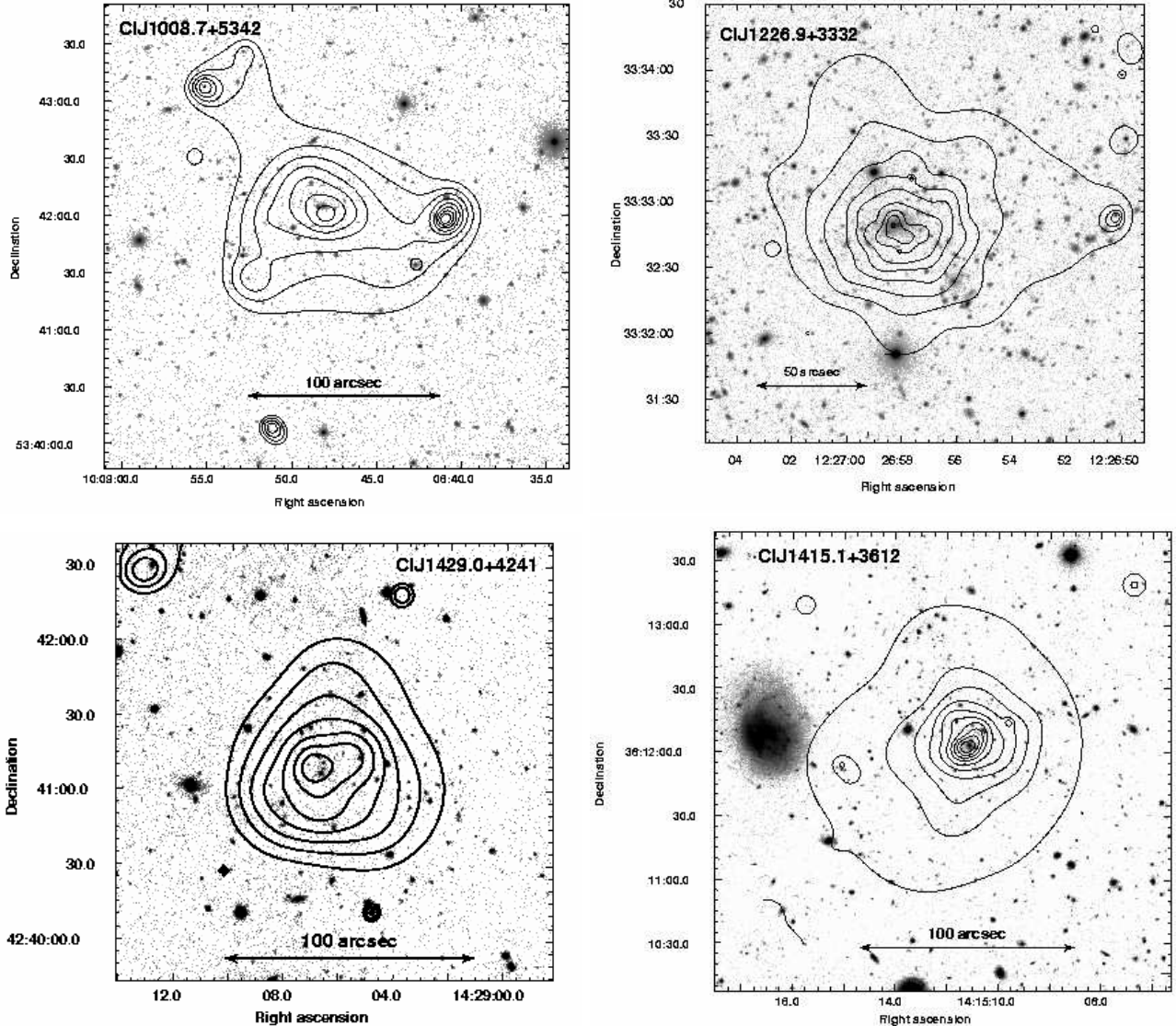


Figure 2. Contours of X-ray emission overlaid on optical images of the WARPS high-redshift sample. The pass-bands and telescopes used to produce the optical images varied, with the I, R or Z band, and Keck-II, the 4.2m William-Herschel Telescope, Subaru or the University of Hawaii's 2.2m telescope used. Contours are taken from images that were adaptively smoothed (using the *asmooth* algorithm of Ebeling et al. (2005)) such that all features are significant at the 99% level, and are logarithmically spaced, with the lowest contour a factor of 1.5 above the background. The X-ray observatory used, and other information about the clusters is given in Table 1.

observation will allow this massive cluster to be studied in unprecedented detail.

ClJ1429.0+4241. This cluster was observed serendipitously during an *XMM-Newton* observation of the BL Lac H1426+428. Only the data from the MOS2 detector were useful for its study because the other detectors were in fast timing mode. The cluster's morphology is fairly disturbed, particularly in the centre, with a possible second X-ray peak to the West. During the two-dimensional surface-brightness modeling of this system, it was not possible to constrain the β parameter. This is likely to be due to a combination of the system's morphology, its compactness compared with the *XMM-Newton* PSF, and the relatively shallow imaging with the single MOS detector. The fit was thus performed with β fixed at the canonical value of 0.67, and the errors

quoted on β hereafter are the mean fractional errors of the rest of the sample (9%).

ClJ1415.1+3612. At $z = 1.03$, the most distant cluster in the sample. The *XMM-Newton* data show the morphology to be relaxed. A deep (78 ks) *Chandra* observation (Ebeling et al. in preparation) of this system confirms the relaxed morphology, and rules out significant unresolved point source contamination in the *XMM-Newton* data used here.

The measurement of reliable masses for these clusters based on the X-ray data requires that they be in hydrostatic equilibrium. Five systems (ClJ1342.9+2828, ClJ1103.6+3555, ClJ0152.7-1357N, ClJ1559.1+6353 and ClJ1429.0+4241) are possibly unrelaxed showing disturbed morphologies, possible substructure and/or large elliptici-

Cluster	z	satellite	exposure (ks)	r_d^{\dagger} ('')	$(R_{2500(z)})$	$(R_{200(z)})$	scale (kpc/ '')	kT (keV)	Z (Z_{\odot})	r_c (kpc)	β	e
ClJ0046.3+8530 ^a	0.62	X	44	88	2.5	0.63	6.81	$4.4^{+0.5}_{-0.4}$	$0.61^{+0.22}_{-0.19}$	137^{+30}_{-25}	$0.60^{+0.08}_{-0.03}$	0.07
ClJ1342.9+2828	0.71	X	33	109	4.3	0.89	7.19	$3.7^{+0.5}_{-0.4}$	$0.19^{+0.22}_{-0.19}$	172^{+28}_{-24}	$0.70^{+0.06}_{-0.05}$	0.34
ClJ1113.1-2615 ^b	0.73	C	65	50	1.4	0.37	7.24	$4.7^{+0.9}_{-0.7}$	$0.71^{+0.40}_{-0.31}$	106^{+9}_{-16}	$0.67^{+0.03}_{-0.05}$	0.20
ClJ1103.6+3555	0.78	X	36	95	2.9	0.72	7.43	$6.0^{+0.9}_{-0.7}$	$0.42^{+0.27}_{-0.21}$	141^{+21}_{-16}	0.58 ± 0.03	0.18
ClJ0152.7-1357N ^b	0.83	C	31	49	2.5	0.37	7.61	$5.6^{+1.0}_{-0.8}$	$0.33^{+0.27}_{-0.23}$	249^{+63}_{-33}	$0.73^{+0.13}_{-0.06}$	0.08
ClJ0152.7-1357S ^b	0.83	C	31	37	1.3	0.31	7.61	$4.8^{+1.1}_{-1.0}$	$0.19^{+0.52}_{-0.19}$	123^{+28}_{-20}	$0.66^{+0.08}_{-0.06}$	0.00
ClJ1559.1+6353	0.85	X	19	73	2.6	0.72	7.54	$4.1^{+1.4}_{-1.0}$	$1.30^{+0.70}_{-0.70}$	67^{+34}_{-25}	$0.59^{+0.06}_{-0.11}$	0.35
ClJ1008.7+5342	0.87	X	14	98	5.4	1.00	7.72	$3.6^{+0.8}_{-0.6}$	$0.11^{+0.43}_{-0.11}$	170^{+47}_{-39}	$0.68^{+0.08}_{-0.10}$	0.27
ClJ1226.9+3332 ^c	0.89	X	17	100	2.2	0.60	7.76	$10.6^{+1.1}_{-1.1}$	$0.49^{+0.17}_{-0.17}$	113^{+9}_{-6}	$0.66^{+0.02}_{-0.02}$	0.14
ClJ1429.0+4241	0.92	X	44	50	1.5	0.40	7.84	$6.2^{+1.5}_{-1.0}$	$0.49^{+0.55}_{-0.44}$	97 ± 9	$0.67 \pm 0.06^{\ddagger}$	0.16
ClJ1415.1+3612	1.03	X	17	60	2.1	0.55	8.06	$5.7^{+1.2}_{-0.7}$	$0.45^{+0.39}_{-0.33}$	94^{+19}_{-14}	$0.67^{+0.06}_{-0.04}$	0.16

Table 1. Summary of the observed properties of the WARPS high-redshift sample. Column 3 indicates whether the observation used here was made with *Chandra* (C) or *XMM-Newton* (X). Column 4 gives the on-axis exposure time remaining after removal of high-background periods (the mean of the MOS and PN times is given for *XMM-Newton* observations). Detailed analyses of several of the clusters can be found in ^aMaughan et al. (2004), ^bMaughan et al. (2003) and ^cMaughan et al. (2004). [†]The detection radius is given in units of $R_{2500(z)}$ and $R_{200(z)}$ for each cluster. These radii are defined in §4 and given in Table 2. [‡]The value of β for this cluster was fixed at 0.67 during the surface-brightness fitting, and the error quoted here is the mean fractional error on β in the rest of the sample.

ties. The mass estimates for these systems are thus likely to be less reliable than those for the more relaxed systems.

3.1 Comparison of *Chandra* and *XMM-Newton* Temperatures

In compiling a sample which includes observations performed with two different instruments, the accuracy of their cross-calibration is an important consideration. In particular, for the study of scaling relations, it is important that no systematic bias in the measured temperature is present due to the imperfect calibration of either instrument. For 4 of the clusters in the sample (ClJ0152.7-1357N, ClJ0152.7-1357S, ClJ1226.9+3332 and ClJ1415.1+3612) observation made with both *Chandra* and *XMM-Newton* were available to us. This enabled us to measure temperatures in a consistent way with both observatories. The measured temperatures are plotted in Fig. 3.

While limited by the small number of comparison points and the size of the statistical uncertainties on the temperatures, Fig. 3 suggests no gross systematic disagreement between the *Chandra* and *XMM-Newton* temperatures. This evidence, along with the good agreement between the WARPS L – T relation and the *Chandra* L – T relation of Vikhlinin et al. (2002) (discussed in detail in §6.1) indicate that the cross calibration of the two satellites is not a significant problem in this work. In studies of nearby clusters with high quality observations, some systematic temperature disagreements between *Chandra* and *XMM-Newton* have been found (e.g. Sanderson et al. 2004; Vikhlinin et al. 2005). Given the evidence above, it appears that any such effect is small compared to the statistical uncertainties in this work.

4 CLUSTER SCALING THEORY

When comparing integrated cluster properties such as luminosity and mass with theoretical predictions, simulations, or other work, the radius within which the properties are measured is of great importance. It is common to use a fixed physical size as an outer radius, which has obvious benefits

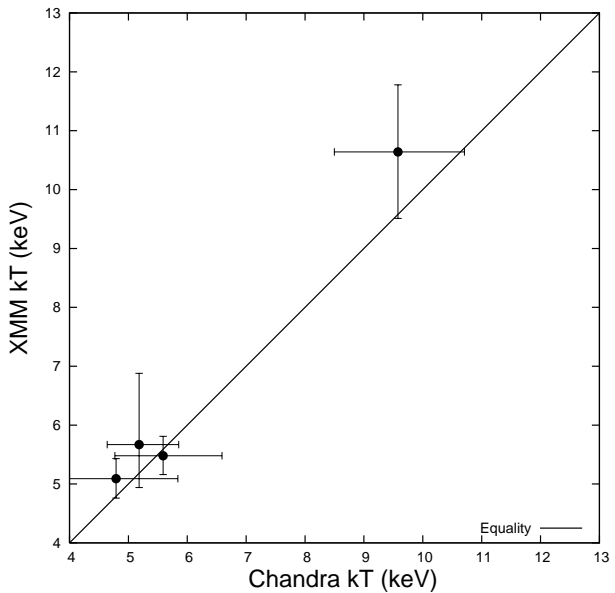


Figure 3. Comparison of temperatures measured with *Chandra* and *XMM-Newton* for the four clusters in our sample observed by both.

in terms of simplicity. A more sophisticated method is to define a radius with some knowledge of the cluster's mass profile so that the mean enclosed density is a fixed factor above the critical density of the universe. This method is more appropriate for comparisons with theoretical predictions, which predict the outer boundary of the virialised part of clusters in terms of a density contrast (Δ_v). For instance, in an Einstein-de Sitter universe, the mean density of virialised systems is $\Delta_v = 18\pi^2 \rho_c$ at all redshifts (e.g. Bryan & Norman 1998). However, the value of Δ_v and its variation with redshift are cosmology dependent (as, of course, is $\rho_c(z)$). Bryan & Norman (1998) calculate the redshift dependence of Δ_v in a Λ CDM cosmology for clusters which

have just virialised, fitting the solution with the expression

$$\Delta_v(z) = 18\pi^2 + 82(\Omega_m(z) - 1) - 39(\Omega_m(z) - 1)^2, \quad (1)$$

where $\Omega_m(z) = \Omega_M(1+z)^3/E(z)^2$, and $E(z)$ describes the redshift evolution of the Hubble parameter, given by

$$E^2(z) = \Omega_M(1+z)^3 + (1 - \Omega_M - \Omega_\Lambda)(1+z)^2 + \Omega_\Lambda. \quad (2)$$

Equation 1 is accurate to within 1% in the range $0.1 \leq \Omega(z) \leq 1$ (Bryan & Norman 1998), which corresponds to all z for $\Omega_M = 0.3$.

The ideal method to follow would therefore be to measure cluster properties within radii corresponding to $\Delta_v(z)$ at all redshifts. This is not possible because X-ray measurements typically only extend to a fraction of the radius corresponding to $\Delta_v(z)$, even at low redshifts, requiring the extrapolation of measured properties by large factors. An alternative to this extrapolation is to work at a smaller radius, corresponding to a higher density contrast, $\Delta(0)$, at $z = 0$. In the self-similar model, this contrast will scale with redshift according to

$$\Delta(z) = \Delta(0) \frac{\Delta_v(z)}{\Delta_v(0)}. \quad (3)$$

In our analysis, all cluster properties are extrapolated to several different radii to enable comparison with other work. We note that for comparison with self-similar models, properties measured within a redshift-dependent density contrast are the most appropriate. In order to simplify the notation, integrated quantities with a numerical subscript, say $M_{\Delta(z)}$, refer to that quantity within a radius ($R_{\Delta(z)}$) enclosing a mean density of $\Delta(z)\rho_c(z)$. For example, $M_{200(z)}$ refers to the mass within a radius enclosing a mean overdensity of 200 at $z = 0$, and some higher mean overdensity (given by Equation 3) at higher redshifts. Note that this use of a redshift-dependent density contrast to define radii differs from the methods used in our previously published studies of some of these clusters. In Maughan et al. (2004) and Maughan et al. (2004), fixed (redshift-independent) density contrasts were used, while in Maughan et al. (2003) the virial radii were estimated from the temperatures of the clusters. The values of integrated cluster properties quoted in this paper thus differ from those given in the previous studies.

Under the self-similar model, with the assumptions that clusters are spherically symmetric systems and that they virialised at the redshift of observation (late formation), simple scaling relations between cluster properties can be derived, based on the virial theorem (*e.g.* Bryan & Norman 1998). The total gravitating mass within a radius $R_{\Delta(z)}$ is related to the gas temperature by

$$M_{\Delta(z)}E(z)\Delta(z)^{1/2} \propto kT^{3/2} \quad (4)$$

and the gas mass within $R_{\Delta(z)}$ is given by the relation,

$$M_g \Delta(z)E(z)\Delta(z)^{1/2} \propto kT^{3/2}f_{\text{gas}}. \quad (5)$$

If the relative distribution of gas and dark matter does not change with redshift or temperature, *i.e.* the gas-mass fraction f_{gas} is independent of z and kT , then Equation 5 becomes similar to Equation 4. This assumption is supported by measurements of f_{gas} in high-redshift clusters that are consistent with those in local clusters (*e.g.* Allen et al. 2002; Maughan et al. 2004). However, it has been found that f_{gas} is lower in clusters with temperatures below $\sim 3 - 4$ keV

(Sanderson et al. 2003, hereafter S03), which may invalidate the assumption of invariant f_{gas} for those systems.

Under the additional assumption that clusters emission is dominated by bremsstrahlung in the X-ray band (a reasonable assumption at the temperatures considered here), the X-ray luminosity within $R_{\Delta(z)}$ is given by

$$L_{\Delta(z)}E(z)^{-1}\Delta(z)^{-1/2} \propto kT^2f_{\text{gas}}^2. \quad (6)$$

The scaling between total mass and X-ray luminosity (M – L relation) is then given by combining Equations 4 and 6, yielding

$$L_{\Delta(z)}E(z)^{-7/3}\Delta(z)^{-7/6} \propto M_{\Delta(z)}^{4/3}f_{\text{gas}}^2. \quad (7)$$

5 SUMMARY OF CLUSTER PROPERTIES AND LINE-FITTING METHODS

The methods used to derive the properties of the clusters in the sample can be summarised as follows. Overdensity radii $R_{\Delta(z)}$ were measured as described in §2. The luminosities measured within r_d were extrapolated to $R_{\Delta(z)}$ using the best-fitting surface-brightness profiles. The fractional detection radius $r_d/R_{200(z)}$ varied from 0.3 to 0.9, while $r_d/R_{2500(z)}$ was greater than unity for all clusters (see Table 1). The luminosities were thus scaled from r_d to $R_{200(z)}$ by factors in the range 1.0 – 1.5 (median= 1.1).

Similarly, the gas masses were derived at different $R_{\Delta(z)}$ by extrapolation of the gas-mass profiles, obtained from the surface-brightness profiles. The extrapolation factors of M_{gas} from r_d to $R_{200(z)}$ were in the range 1.1 – 5.3 with a median of 1.9. The total-mass profiles were used to derive the total masses at different overdensity radii, being scaled up by a factor in the range 1.1 – 3.8 (median= 1.7) from r_d to $R_{200(z)}$.

For ClJ0046.3+8530 and ClJ1226.9+3332, temperature profiles and hardness-ratio maps support the isothermal assumption to at least $0.6R_{200(z)}$. The effect of possible departures from isothermality is investigated below.

To enable comparisons with other work, the integrated properties of the WARPS sample are summarised in Table 2, derived within different radii.

The observed properties of the WARPS sample, and others, are compared with the predicted scaling relations in the following sections. The best-fitting scaling relations to the observations were found by performing an orthogonal, weighted “BCES” regression (as described by Akritas & Bershady 1996), on the data in log space. This method takes into account measurement errors on both variables, correlations in those errors, and intrinsic scatter in the data. The use of orthogonal regression avoids the biases inherent in bisector-regression fits to data with intrinsic scatter. The errors on the slopes and normalisations of the relations were derived from jackknife analyses of the datasets. The χ^2 goodness of fit values of the various relations were computed including the errors in both the x and y directions. In a similar way, the intrinsic scatter (σ_s) of the data about the relations was defined in log space as

$$\sigma_s = \frac{1}{N} \sum_{i=1}^N \left[\frac{(y_i - mx_i - c)^2}{\sigma_{y_i}^2 + m^2\sigma_{x_i}^2} \right]^{1/2}, \quad (8)$$

where m and c are the gradient and intercept of the relation,

Cluster	z	kT keV	$R_{200(z)}$ Mpc	$L_{200(z)}$ 10^{44} erg s $^{-1}$	M_g $200(z)$ $10^{13} M_\odot$	$M_{200(z)}$ $10^{14} M_\odot$	$R_{2500(z)}$ Mpc	$L_{2500(z)}$ 10^{44} erg s $^{-1}$	M_g $2500(z)$ $10^{12} M_\odot$	$M_{2500(z)}$ $10^{13} M_\odot$
ClJ0046.3+8530	0.62	$4.4^{+0.5}$	$0.96^{+0.06}$	$4.11^{+0.23}$	$3.69^{+0.34}$	$2.81^{+0.59}$	$0.24^{+0.02}$	$2.01^{+0.35}$	$3.74^{+0.86}$	$5.29^{+1.46}$
ClJ1342.9+2828 †	0.71	$3.7^{+0.4}$	$0.88^{+0.06}$	$3.52^{+0.14}$	$3.08^{+0.32}$	$2.46^{+0.59}$	$0.18^{+0.02}$	$1.50^{+0.36}$	$2.27^{+0.83}$	$2.86^{+1.28}$
ClJ1113.1-2615	0.72	$4.7^{+0.9}$	$0.97^{+0.09}$	$3.85^{+0.32}$	$2.92^{+0.35}$	$3.39^{+1.02}$	$0.26^{+0.02}$	$2.69^{+0.26}$	$4.75^{+0.94}$	$7.75^{+2.59}$
ClJ1103.6+3555 †	0.78	$6.0^{+0.9}$	$0.98^{+0.07}$	$4.98^{+0.22}$	$4.06^{+0.45}$	$3.82^{+0.88}$	$0.24^{+0.02}$	$2.30^{+0.31}$	$3.92^{+0.89}$	$7.22^{+2.09}$
ClJ0152.7-1357N †	0.83	$5.6^{+1.0}$	$1.00^{+0.10}$	$11.50^{+1.52}$	$6.48^{+1.37}$	$4.33^{+1.54}$	$0.15^{+0.05}$	$2.62^{+1.58}$	$1.77^{+2.11}$	$1.90^{+2.48}$
ClJ0152.7-1357S	0.83	$4.8^{+1.1}$	$0.90^{+0.10}$	$6.72^{+1.07}$	$3.84^{+0.80}$	$3.14^{+1.22}$	$0.22^{+0.03}$	$3.96^{+0.57}$	$4.86^{+1.38}$	$6.16^{+3.06}$
ClJ1559.1+6353 †	0.85	$4.1^{+1.0}$	$0.78^{+0.14}$	$2.59^{+0.33}$	$1.92^{+0.51}$	$2.12^{+1.00}$	$0.21^{+0.04}$	$1.68^{+0.46}$	$2.86^{+1.13}$	$5.28^{+3.72}$
ClJ1008.7+5342	0.87	$3.6^{+0.8}$	$0.76^{+0.08}$	$3.84^{+0.28}$	$2.74^{+0.47}$	$2.00^{+0.81}$	$0.14^{+0.04}$	$1.16^{+0.70}$	$1.23^{+1.15}$	$1.57^{+1.56}$
ClJ1226.9+3332	0.89	$10.6^{+1.1}$	$1.29^{+0.06}$	$43.70^{+0.96}$	$11.90^{+0.89}$	$10.20^{+1.71}$	$0.35^{+0.02}$	$32.70^{+1.39}$	$21.50^{+1.93}$	$25.00^{+4.61}$
ClJ1429.0+4241 †	0.92	$6.2^{+1.5}$	$0.97^{+0.11}$	$9.59^{+0.92}$	$4.29^{+0.76}$	$4.49^{+1.73}$	$0.26^{+0.03}$	$6.92^{+0.70}$	$7.28^{+1.53}$	$10.50^{+4.77}$
ClJ1415.1+3612	1.03	$5.7^{+1.2}$	$0.88^{+0.08}$	$10.40^{+0.62}$	$3.85^{+0.54}$	$3.83^{+1.20}$	$0.23^{+0.02}$	$7.58^{+0.70}$	$6.73^{+1.22}$	$8.82^{+3.12}$

Table 2. Summary of the integrated properties of the WARPS high-redshift sample derived within different radii. Luminosities are bolometric X-ray luminosities. † These systems show evidence of being unrelaxed

and (x_i, y_i) are the coordinates of each of the N data points, with uncertainties $(\sigma_{xi}, \sigma_{yi})$. This measurement was used to compare the scatter in the different relations discussed here.

6 THE L – T RELATION

The effect of cool cores needs to be accounted for in any measurement of the L – T relation. Many relaxed clusters have dense cooling cores, with gas temperatures in the central ~ 100 kpc falling to $\sim 1/3$ of the global temperature, and sharply peaked surface-brightness profiles (e.g. Fabian 1994; Kaastra et al. 2001). These effects are not included in the self-similar model, so must be taken into account in the analysis. This is routinely done by excluding the central region of such clusters from the analyses. None of the clusters in our sample showed significant evidence for cooling cores; where temperature profiles and hardness-ratio maps could be created (ClJ0046.3+8530 and ClJ1226.9+3332) there was no indication of cooler gas in the central regions, and none of the surface-brightness profiles were centrally peaked. For this reason, no cooling-core correction was applied to the luminosities or temperatures of the high-redshift clusters.

If the L – T relation evolves as predicted by Equation 6, then the effect of evolution can be removed by dividing the luminosity of each cluster by $E(z)^{-1}(\Delta(z)/\Delta(0))^{-1/2}$, which reduces to $E(z)^{-1}(\Delta_v(z)/\Delta_v(0))^{-1/2}$. Following this scaling, the high-z clusters should lie on the local relation. Of the two factors describing the evolution, $E(z)$ dominates; at $z = 1$, $E(z)^{-1} = 0.57$ and $(\Delta_v(z)/\Delta_v(0))^{-1/2} = 0.80$. Fig. 4 shows the scaled luminosities (those with self-similar evolution factored out) measured within $R_{200(z)}$ plotted against temperature. A relation of the form

$$E(z)^{-1} \left(\frac{\Delta_v(z)}{\Delta_v(0)} \right)^{-1/2} L_{\Delta(z)} = A \left(\frac{kT}{6 \text{ keV}} \right)^B \quad (9)$$

was fit to the data, resulting in best-fit values $A = (5.14 \pm 0.84) \times 10^{44} h_{70}^{-2}$ erg s $^{-1}$, $B = 2.78 \pm 0.55$. The dot-dashed line in Fig. 4 shows the best-fitting relation with the observed luminosities, illustrating the effect of the predicted evolution.

Also plotted on Fig. 4 is the local L – T relation measured by Arnaud & Evrard (1999, hereafter AE99) for a sample of clusters with little or no central cooling. It is unclear

within what precise radius the AE99 luminosities were determined, however as they are referred to as “total luminosities” we assume they are derived within $R_{200(z)}$. If the AE99 luminosities were extrapolated to some larger radius (or to infinity), then the luminosities will be $\lesssim 10\%$ higher than the values within $R_{200(z)}$. The best fit to our scaled high-redshift data is consistent, within the errors, with the parameters for the local relation of $A = (5.86 \pm 0.40) \times 10^{44} h_{70}^{-2}$, $B = 2.88 \pm 0.15$. The local AE99 relation provides an acceptable fit to the scaled high-redshift data ($\chi^2/\nu = 10.2/9$), while the unscaled high-redshift data rule out the local relation at $> 95\%$ level ($\chi^2/\nu = 18.9/9$).

The scaled WARPS high-z L – T relation is also compared with the local relation measured by Markevitch (1998) in Fig. 4. In contrast with AE99, Markevitch (1998) corrected for central cooling by excising the central regions of the clusters and extrapolating a surface-brightness profile over this region. The luminosities measured by Markevitch (1998) were extrapolated to a fixed radius of $1.4h_{70}^{-1}$ Mpc, so are expected to be $\approx 2\%$ higher than the values derived within $R_{200(z)}$ (based on the typical scaling of luminosity from $1.4h_{70}^{-1}$ Mpc to $R_{200(z)}$ for our sample). The best-fitting relation found by Markevitch (1998) has $A = (6.35 \pm 0.55) \times 10^{44} h_{70}^{-2}$ and $B = 2.64 \pm 0.27$ in our notation. While the WARPS data are also reasonably consistent with this local relation ($\chi^2/\nu = 14.2/9$), we prefer to compare the results with AE99 because the treatment of central cooling is consistent.

6.1 Comparison with Vikhlinin et al. (2002)

The results for the WARPS sample was compared with those obtained by Vikhlinin et al. (2002, hereafter V02) for a sample consisting of 22 clusters at $z > 0.4$ observed with *Chandra*. In the V02 sample, luminosities were extrapolated to a fixed radius of $1.4h_{70}^{-1}$ Mpc irrespective of their redshift. In order to compare the V02 luminosities with self-similar predictions, they were scaled to $R_{200(z)}$. The value of $R_{200(z)}$ was computed in an identical way to the WARPS clusters (see §2) using the values of z , kT , r_c and β given by V02. Random realisations of the overdensity profiles were computed from the uncertainties on z , kT , β , given by V02. The luminosity of each system was then scaled from $1.4h_{70}^{-1}$ Mpc to $R_{200(z)}$ based on β -profiles with the parameters given by

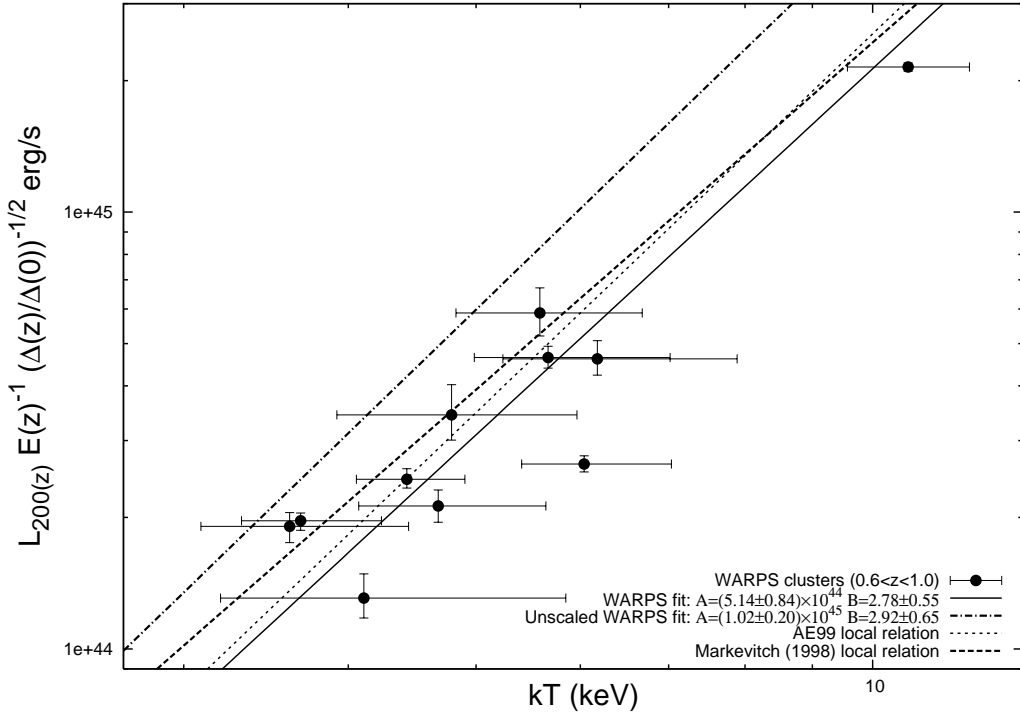


Figure 4. L – T relation for the high-redshift WARPS sample. Luminosities were extrapolated to a radius $R_{200(z)}$, corresponding to a redshift-dependent density contrast 200, and scaled by a factor of $E(z)^{-1}[\Delta(z)/\Delta(0)]^{-1/2}$ as predicted by the self-similar model. The solid line is the best fit to the data, and the dotted and dashed lines are the local relations of AE99 and Markevitch (1998) respectively. The dot-dashed line is the best fit to the unscaled high-redshift clusters (points not plotted) and can be used to judge the significance of the self-similar scaling.

V02 for that cluster. The resulting scale factors for the luminosities were close to unity, ranging from 0.89 to 1.02 with a mean of 0.98.

As no errors on L_X are given by V02, the mean fractional uncertainty from the WARPS sample of 0.09 was assumed for the V02 clusters. The errors on the luminosities scaled to $R_{200(z)}$ thus include the statistical uncertainties in modeling the overdensity profiles, and an additional 9% uncertainty.

V02 excluded the central $71h_{70}^{-1}$ kpc of clusters which had peaked surface-brightness profiles, and extrapolated over that region to correct for central cooling effects. As no cooling corrections were applied to the WARPS clusters, the corrected clusters were discarded from the V02 sample (this is a fairly conservative move as the corrected clusters do not scatter from the V02 L – T relation). We also excluded ClJ0152.7–1357, which is already in the WARPS sample, leaving 13 V02 clusters. The best-fitting L – T relation for those clusters was consistent with the WARPS L – T relation shown in Fig. 4. The two samples were then combined to give a sample of 22 systems, with 16 at $z > 0.6$. The luminosities were scaled as before to remove the predicted self-similar evolution, and the resulting L – T relation is shown in Fig. 5, along with the local AE99 relation.

The best-fitting parameters for the joint sample are $A = (6.24 \pm 0.62) \times 10^{44}h_{70}^{-2}$ and $B = 3.32 \pm 0.37$. This is marginally consistent with the local AE99 relation, with $\chi^2/\nu = 33.3/22$. However, this statistic does not take into account any intrinsic scatter in the data so the null hypoth-

esis probability of 6% is an underestimate to some extent. We thus conclude that the scaled high-redshift data cannot exclude the local AE99 relation as an acceptable model. Comparison of the *unscaled* data for the combined WARPS and V02 samples (indicated by the dot-dashed line in Fig. 5) with the AE99 relation strongly rules out the local relation as a description of the high-redshift data ($\chi^2/\nu = 130/22$).

As the WARPS results are based mainly on *XMM-Newton* observations, a potential source of systematic error is that cooling cores in high-redshift systems could go undetected due to the large PSF of *XMM-Newton*. However, the best-fitting relation for the combination of the WARPS sample and the V02 data (excluding the systems with cooling cores detected by *Chandra*) is a good description of both samples (Fig. 5). Both samples also show a similar amount of scatter about the best-fitting relation. This suggests that the *XMM-Newton* measurements were not contaminated by undetected cooling cores, and that the cross-calibration of the instruments is not a significant concern here.

6.2 Comparison with Ettori et al. (2004)

The WARPS sample was then compared with the larger, more recently compiled sample of Ettori et al. (2004, hereafter E04) which comprises 28 clusters at $z > 0.4$ from the *Chandra* archive. In E04, luminosities were extrapolated to $R'_{500(z)}$, where the prime indicates a slightly different definition of $\Delta(z)$ used in that work. The density contrast in E04

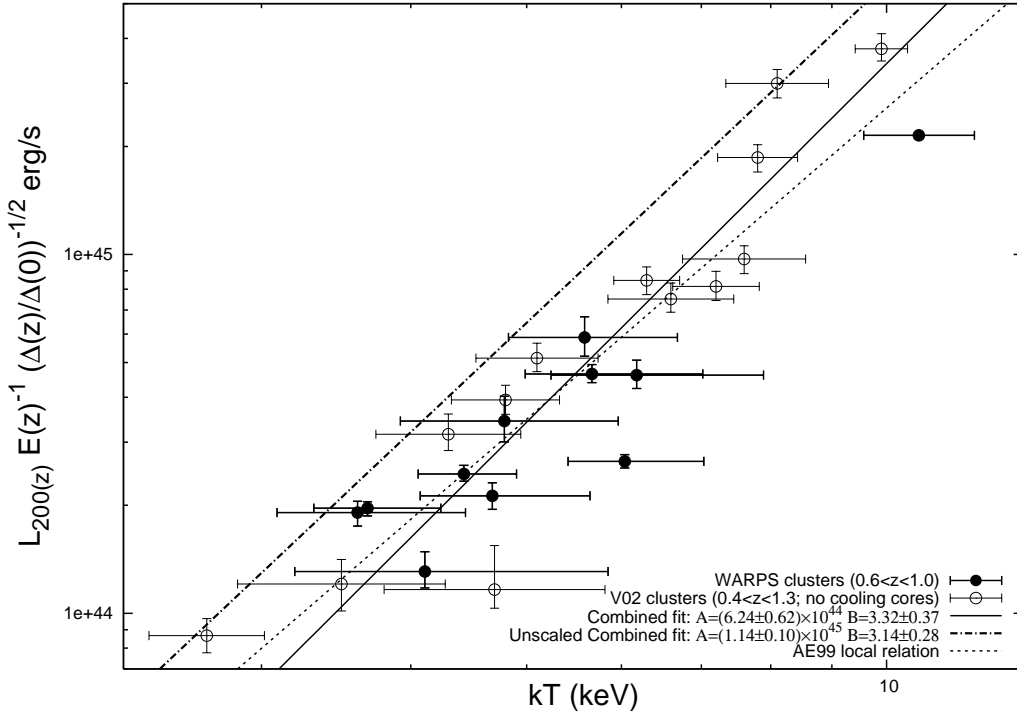


Figure 5. L – T relation for the combined WARPS and V02 samples. The WARPS data are the same as in Fig. 4. The V02 data were treated in the same way, with L_X extrapolated to $R_{200(z)}$ and scaled by $E(z)^{-1}[\Delta(z)/\Delta(0)]^{-1/2}$. The solid line is the best fit to the combined dataset.

was defined as

$$\Delta'(z) = 500 \frac{\Delta_v(z)}{18\pi^2}, \quad (10)$$

so is related to our $\Delta(z)$ by

$$\Delta'(z) = \frac{\Delta_v(0)}{18\pi^2} \Delta(z). \quad (11)$$

In the case of an Einstein-de Sitter universe $\Delta'(z) = \Delta(z)$. In our assumed low-density Λ CDM cosmology however, $\Delta_v(0)/18\pi^2 = 1.76$ and so $\Delta'(z) < \Delta(z)$, leading to higher measured luminosities within $R'_{500(z)}$. This change in definition thus introduces a redshift-independent change in all luminosities, but the predicted evolution of the L – T relation is unaffected. For consistency with E04, the luminosities of the WARPS clusters were extrapolated to $R'_{500(z)}$. The resulting WARPS L – T relation is plotted along with the E04 relation in Fig. 6. The AE99 relation is also plotted for comparison, though it should be recalled that those luminosities were extrapolated to larger radii. In addition to any evolution, the normalisation of the AE99 relation should thus be $\approx 5\%$ higher than the $R'_{500(z)}$ relations (estimated from the extrapolation of a standard β -profile from $R'_{500(z)}$ to $R_{200(z)}$).

The best fit to the WARPS $R'_{500(z)}$ L – T relation is consistent with the $R_{200(z)}$ relation of Fig. 4, and the local AE99 relation (see Table 3). The best fit to the E04 relation, with $A = (5.2 \pm 1.1) \times 10^{44} h_{70}^{-2}$ and $B = 4.28 \pm 0.60$, is possibly steeper than the other L – T relations discussed here (at the $\sim 2\sigma$ level). We note that the slope we measure for the E04 sample is steeper than that quoted in E04 ($B = 3.72 \pm 0.47$). This is because we have scaled the luminosities

by $E(z)^{-1}(\Delta_v(z)/\Delta_v(0))^{-1/2}$ whereas E04 scaled by $E(z)^{-1}$ alone, and because we use an orthogonal BCES regression, while E04 used a bisector BCES regression. If we eliminate these two differences, we recover the same fit as E04.

The scatter of the E04 data about the best-fit L – T relation is $\sigma_s = 1.78$ which is larger than that of the combined WARPS and V02 sample ($\sigma_s = 0.85$; *c.f.* Figs. 5 and 6). One probable cause of this is that E04 made no correction for cool cores, while 7 of the clusters were classed as having cool cores by V02. These cool core clusters are indicated in Fig. 6, and their exclusion reduces both the scatter ($\sigma_s = 1.25$) and also the normalisation of the best fitting relation. In light of these differences, and the good agreement between the WARPS and V02 L – T relations, we prefer to use the combined WARPS and V02 L – T relation, with luminosities measured within $R_{200(z)}$ in our further discussions. The different L – T relations discussed in this section are summarised in Table 3.

7 THE M – T RELATION

In the self-similar evolution scenario, assuming the late-formation approximation, the M – T relation is given by Equation 4. The evolution of the M – T relation was investigated by comparing the WARPS sample to the local sample of S03, which comprises 66 clusters with reliable masses derived from temperature and surface-brightness profiles. We chose S03 for this comparison because the overdensity radii and mass measurements were made in the same way as in this work. Importantly, S03 also derived total and gas masses for all of the clusters in their sample under the assumption

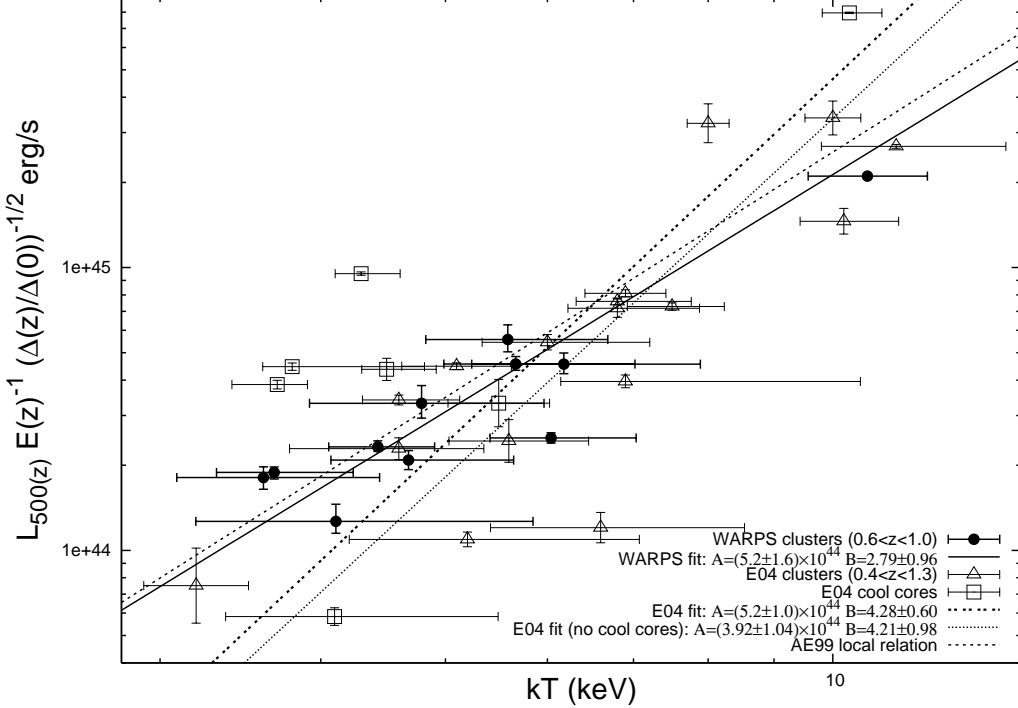


Figure 6. L – T relations of the WARPS and E04 samples. Luminosities were extrapolated to $R'_{500(z)}$.

L – T relation	$A (10^{44} h_{70}^{-2} \text{ erg s}^{-1})$	B	notes
Luminosities extrapolated to $R_{200(z)}$			
AE99	5.86 ± 0.40	2.88 ± 0.15	Local clusters with no strong central cooling (Fig. 4).
Markevitch (1998)	6.35 ± 0.55	2.64 ± 0.27	Local relation, corrected for cooling cores (Fig. 4).
WARPS	5.14 ± 0.84	2.78 ± 0.55	$0.6 < z < 1.0$ clusters with no cooling cores (Fig. 4).
V02 & WARPS	6.24 ± 0.62	3.32 ± 0.37	Combined samples ($0.4 < z < 1.3$), no cooling cores (Fig. 5).
Luminosities extrapolated to $R'_{500(z)}$			
E04	5.21 ± 1.05	4.28 ± 0.60	Full E04 $0.4 < z < 1.3$ sample (Fig. 6).
E04 (no cool cores)	3.92 ± 1.04	4.21 ± 0.98	E04 $0.4 < z < 1.3$ clusters with no cooling cores (Fig. 6).
WARPS ($R'_{500(z)}$)	4.97 ± 0.80	2.80 ± 0.55	WARPS $0.6 < z < 1.0$ clusters with no cooling cores (Fig. 6).

Table 3. Summary of the L – T relations discussed in §6. Luminosities of the high-redshift clusters were scaled by $E(z)^{-1}(\Delta_v(z)/\Delta_v(0))^{-1/2}$ to remove the predicted self-similar evolution.

of isothermality. They found that assuming isothermality for their entire sample, including genuinely isothermal, and non-isothermal clusters lead to an average $\sim 30\%$ overestimate of the true mass (the mass estimated with full temperature profiles) within R_{200} .

This is a key point in this analysis. In all but a few cases, departures from isothermality in the high- z clusters cannot be detected. In the cases where there is evidence in support of isothermality, the constraints are not strong. While some of the high- z systems may be genuinely isothermal, others will surely not be. Assuming isothermality for the whole sample (while correct for some clusters) is likely to lead to an *average* systematic mass overestimate similar to that found by S03. In order to separate this systematic effect from any real evolution in the M – T relation, it is essential that isothermal masses be used for the low-redshift clusters.

For consistency with the WARPS sample, we include only the 40 clusters from the S03 sample with $kT > 3$ keV. The slopes and normalisations of the relations we fit to the S03 data vary from those reported in S03 because of this temperature cut-off, and because we use a slightly different fitting algorithm than S03.

A reliable masses measurement requires that the clusters be in hydrostatic equilibrium. The five possibly unrelaxed high-redshift clusters (ClJ1342.9+2828, ClJ1103.6+3555, ClJ0152.7–1357N, ClJ1559.1+6353 and ClJ1429.0+4241) were flagged in this analysis, and all of the M – T relations were fit with and without these systems. Excluding the unrelaxed systems had no significant effect on any of the best fit relations, and so they were retained to avoid biasing the sample.

Masses were derived within $R_{2500(z)}$, which falls within the detection radius for all of the WARPS clusters, and

$R_{200(z)}$, which corresponds to the estimated virial radius used in many other studies. Similarly to the method used with the L – T relation, the predicted self-similar evolution was factored out of the high-redshift cluster masses by fitting a relation of the form

$$E(z) \left(\frac{\Delta_v(z)}{\Delta_v(0)} \right)^{1/2} M_{\Delta(z)} = A \left(\frac{kT}{6 \text{ keV}} \right)^B \quad (12)$$

to the data.

Fig. 7 shows the $M_{2500(z)} - T$ relation for the S03 and WARPS samples. The masses for both samples were derived assuming isothermality. The temperatures of the S03 clusters are emission-weighted temperatures measured within $0.3R_{200(z)}$, which corresponds closely to $R_{2500(z)}$, and are extrapolated over any central cool gas (see S03). The WARPS temperatures are also emission weighted, and are measured within the clusters' detection radii. These measurements are consistent, under the assumption of isothermality, with the S03 temperature measurements. Our best-fitting relation for the S03 data is given by $A = (1.92 \pm 0.10) \times 10^{14} h_{70}$ and $B = 1.89 \pm 0.15$, while the best-fit to the WARPS data is parameterised by $A = (1.49 \pm 0.23) \times 10^{14} h_{70}$ and $B = 2.01 \pm 0.26$.

The $M_{2500(z)} - T$ relation was also measured for the WARPS systems when their masses were not scaled by the predicted evolution, and is plotted as a dot-dashed line in Fig. 7. These unscaled masses provide strong evidence for evolution of the $M_{2500(z)} - T$ relation; the χ^2 of the local relation to the unscaled high-redshift data is $\chi^2/\nu = 37.3/9$. The scaled high-redshift data agree well with the local isothermal relation, with $\chi^2/\nu = 4.4/9$.

The $M_{200(z)} - T$ relation is shown in Fig. 8 for the S03 and WARPS samples. The temperatures of the S03 clusters are as above, but measured within $R_{200(z)}$, while the WARPS temperatures are again measured within r_d . The isothermal S03 masses were used and the best-fit parameters are summarised in Table 4. Again, the scaled high-redshift data are consistent with the local isothermal relation ($\chi^2/\nu = 2.9/9$). The best-fitting relation for the WARPS data using masses not scaled by the predicted evolution is also plotted in Fig. 8 as a dot-dashed line. The unscaled high-redshift data are inconsistent with the local isothermal $M_{200(z)} - T$ relation ($\chi^2/\nu = 38.8/9$), providing evidence for evolution.

To enable comparisons with other work, masses of the WARPS clusters were also derived within radii enclosing fixed, redshift-independent density contrasts of $\Delta(z) = \Delta(0) = 2500$ and $\Delta(z) = \Delta(0) = 200$. These data were then fit with a relation of the form

$$M_{\Delta(z)} = A \left(\frac{kT}{6 \text{ keV}} \right)^B, \quad (13)$$

so no scaling for the predicted self-similar evolution was made. The best-fitting slopes and normalisations are given in Table 4.

8 THE $M_g - T$ RELATION

The comparison of the WARPS and S03 samples also enabled the investigation of the evolution of the $M_g - T$ relation. The gas mass is less dependent on uncertainties in

the cluster temperature structure than the total mass. This is because the gas density profile is obtained easily from the X-ray surface-brightness profile, and the gas luminosity depends strongly on density (as ρ^2) and weakly on temperature (as $T^{1/2}$). This makes the $M_g - T$ relation potentially a more reliable method of exploring cluster evolution. An incorrect assumption of isothermality would still introduce systematic effects because the definition of overdensity radii depends on the total mass profile. The self-similar $M_g - T$ evolution prediction (Equation 5) is also subject to additional assumptions about the relative distributions of the gas and dark matter (§4).

The $M_g - T$ relations of the S03 and WARPS samples were derived within $R_{2500(z)}$ and $R_{200(z)}$, and are plotted in Figs. 9 and 10 respectively. The predicted self-similar evolution was again factored out of the high-redshift cluster gas masses, with a relation of the form

$$E(z) \left(\frac{\Delta_v(z)}{\Delta_v(0)} \right)^{1/2} M_{g, \Delta(z)} = A \left(\frac{kT}{6 \text{ keV}} \right)^B \quad (14)$$

fit to the data. As with the $M - T$ relation, the unrelaxed clusters in our sample were flagged in this analysis, and the results were found to be independent of their inclusion or exclusion. $M_g - T$ relations were fit to the S03 data, using their gas masses derived under the assumption of isothermality. Table 5 summarises the parameters of the various best-fitting relations.

Measured within $R_{2500(z)}$, the scaled high-redshift and low-redshift $M_g - T$ relations are consistent, with $\chi^2/\nu = 4.8/9$. The scaled high-redshift $M_g - T$ relation within $R_{200(z)}$ is also consistent with the local S03 relation ($\chi^2/\nu = 8.0/9$).

The $M_g - T$ relations for the WARPS clusters when the masses were not scaled by the predicted self-similar evolution are plotted as dot-dashed lines in Figs. 9 and 10. Within both radii, the unscaled high-redshift data are strongly inconsistent with the local isothermal relations, demonstrating the evolution of the relations.

V02 also investigated the evolution of the $M_g - T$ relation, measuring gas masses within an overdensity radius defined in terms of the average baryon density of the universe. Although their measurements are not directly comparable to ours for this reason, they find evidence for weak evolution (with respect to the local relation) in the $M_g - T$ relation that is qualitatively consistent with our results.

9 THE M – L RELATION

The scaling between total mass and X-ray luminosity in the high-redshift clusters was then investigated. The WARPS sample was compared with the low-redshift HIFLUGCS sample of Reiprich & Böhringer (2002) in order to measure any evolution in the M – L relation. The masses and luminosities published in Reiprich & Böhringer (2002) were scaled to $H_0 = 70 \text{ km s}^{-1} \text{ Mpc}^{-1}$, and clusters with $kT < 3 \text{ keV}$ were removed for consistency with the WARPS clusters, leaving 52. The HIFLUGCS sample includes systems regardless of their morphology, although any strong substructure was excluded for the mass and luminosity determinations, and all of the high-redshift clusters (relaxed and unrelaxed) are included in this comparison. In addition,

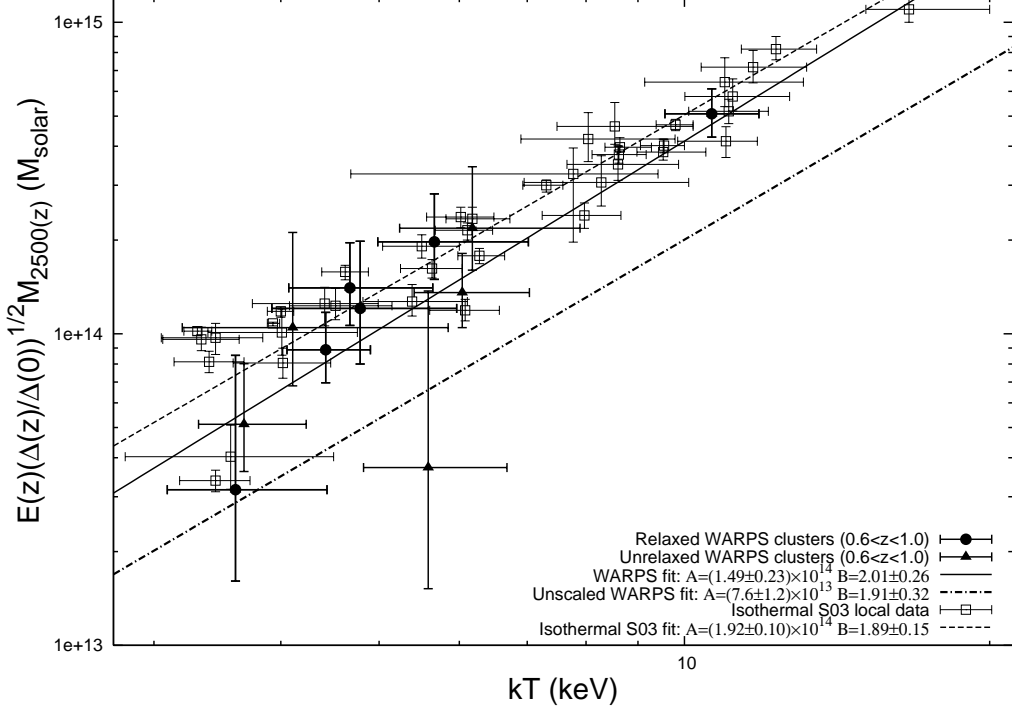


Figure 7. $M_{2500(z)} - T$ relation for the low- z S03 clusters and the relaxed high- z WARPS systems. Masses were measured within $R_{2500(z)}$ assuming isothermality and scaled by the evolution predicted by the self-similar model. The dot-dashed line is the best fit to the unscaled high-redshift clusters (points not plotted) and can be used to judge the significance of the self-similar scaling.

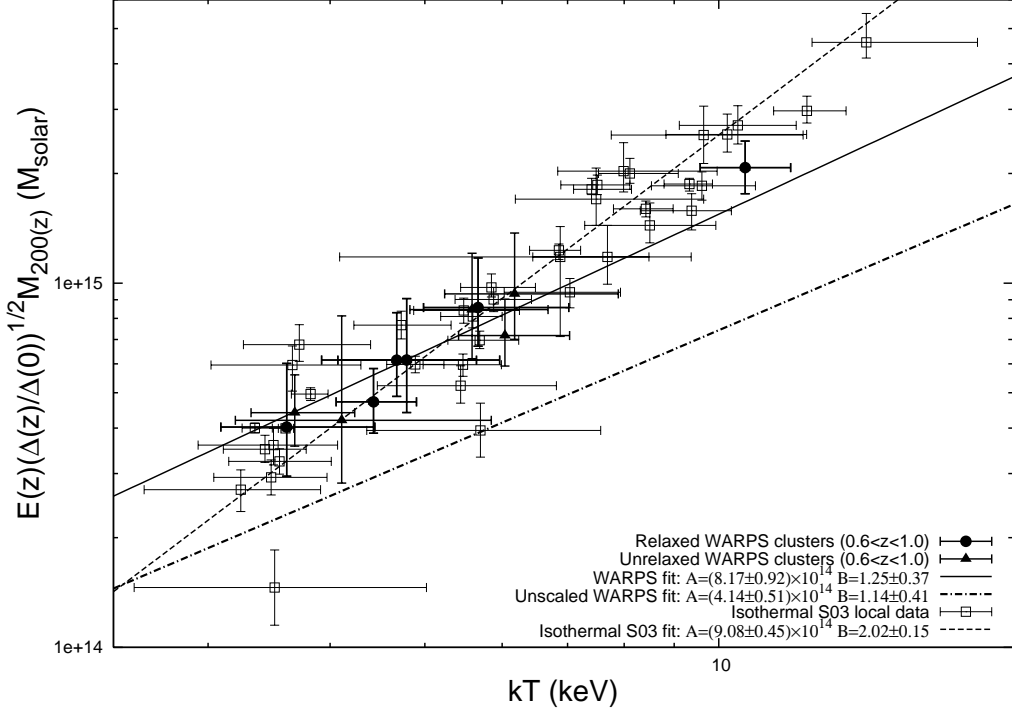


Figure 8. $M_{200(z)} - T$ relation for the low- z S03 clusters and the relaxed high- z WARPS systems. Masses were measured within $R_{200(z)}$ assuming isothermality and scaled by the evolution predicted by the self-similar model. The dot-dashed line is the best fit to the unscaled high-redshift clusters (points not plotted) and can be used to judge the significance of the self-similar scaling.

M – T relation	$A (10^{14} h_{70}^{-1} M_{\odot})$	B	notes
Masses within $R_{2500(z)}$			
WARPS $M_{2500(z)} - T$	1.49 ± 0.23	2.01 ± 0.26	$0.6 < z < 1.0$ clusters, isothermal masses (Fig. 7).
S03 $M_{2500(z)} - T$	1.92 ± 0.10	1.89 ± 0.15	Local clusters, isothermal masses (Fig. 7).
Masses within $R_{200(z)}$			
WARPS $M_{200(z)} - T$	8.17 ± 0.92	1.25 ± 0.37	$0.6 < z < 1.0$ clusters, isothermal masses (Fig. 8).
S03 $M_{200(z)} - T$	9.08 ± 0.45	2.02 ± 0.15	Local clusters, isothermal masses (Fig. 8).
Unscaled masses within redshift-independent density contrast			
WARPS $M_{2500} - T$	1.10 ± 0.19	1.40 ± 0.53	$0.6 < z < 1.0$ clusters, isothermal masses.
WARPS $M_{200} - T$	5.14 ± 0.61	1.16 ± 0.39	$0.6 < z < 1.0$ clusters, isothermal masses.

Table 4. Summary of the M – T relations discussed in §7. Masses of the high-redshift clusters were scaled by $E(z)(\Delta_v(z)/\Delta_v(0))^{1/2}$ to remove the predicted self-similar evolution, with the exception of the bottom section of the table.

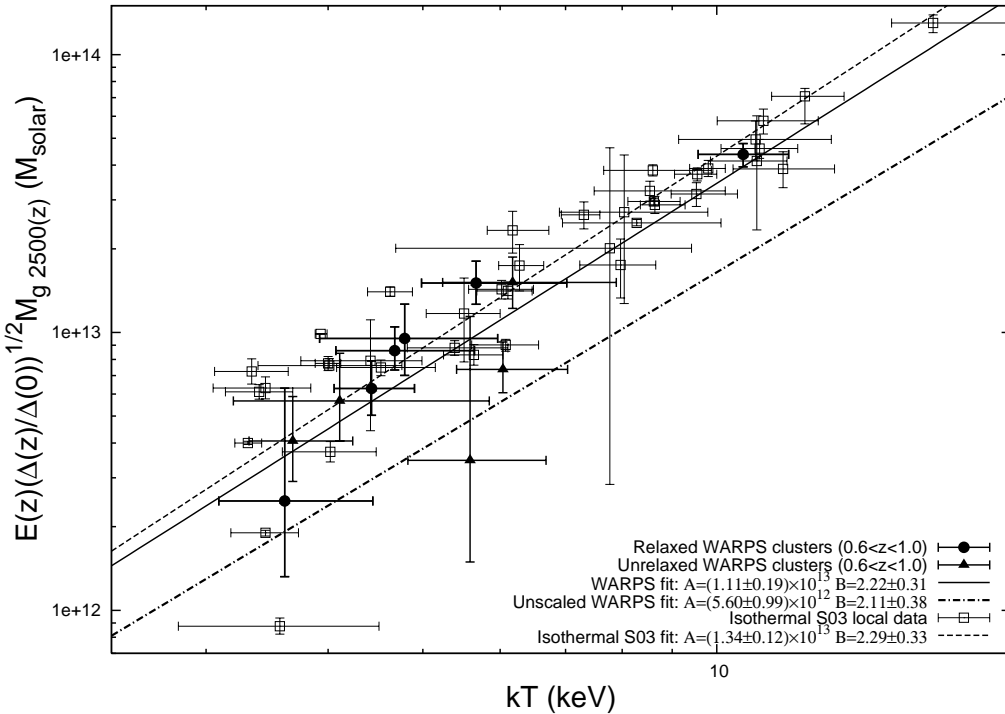


Figure 9. The $M_{g, 2500(z)} - T$ relations of the low-z S03 clusters and relaxed, high-z WARPS systems. Masses were measured within $R_{2500(z)}$ assuming isothermality, and scaled by the evolution predicted by the self-similar model. The dot-dashed line is the best fit to the unscaled high-redshift clusters (points not plotted) and can be used to judge the significance of the self-similar scaling.

$M_g - T$ relation	$A (10^{13} h_{70}^{-1} M_{\odot})$	B	notes
Gas masses within $R_{2500(z)}$			
WARPS $M_{g, 2500(z)} - T$	1.11 ± 0.19	2.22 ± 0.31	$0.6 < z < 1.0$ clusters, isothermal masses (Fig. 9).
S03 $M_{g, 2500(z)} - T$	1.34 ± 0.12	2.29 ± 0.33	Local clusters, isothermal masses (Fig. 9).
Gas masses within $R_{200(z)}$			
WARPS $M_{g, 200(z)} - T$	10.0 ± 1.4	1.80 ± 0.49	$0.6 < z < 1.0$ clusters, isothermal masses (Fig. 10).
S03 $M_{g, 200(z)} - T$	8.80 ± 0.52	2.01 ± 0.26	Local clusters, isothermal masses (Fig. 10).

Table 5. Summary of the $M_g - T$ relations discussed in §8. Masses of the high-redshift clusters were scaled by $E(z)(\Delta_v(z)/\Delta_v(0))^{1/2}$ to remove the predicted self-similar evolution.

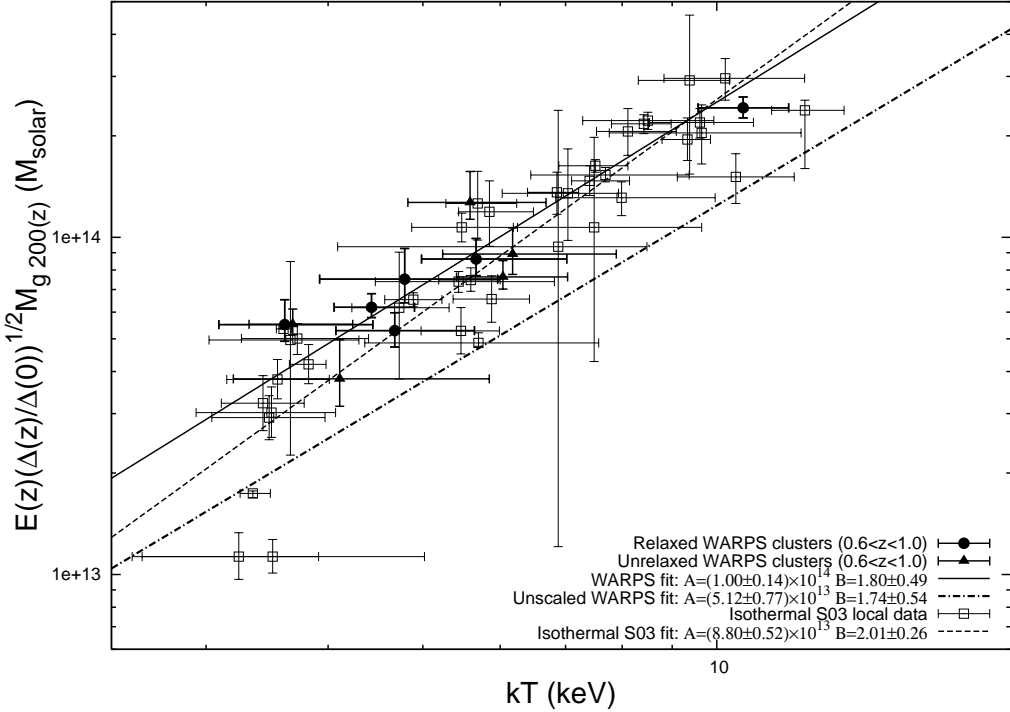


Figure 10. The $M_{g,200(z)}$ – T relations of the low- z S03 clusters and relaxed, high- z WARPS systems. Masses were measured within $R_{200(z)}$ assuming isothermality, and scaled by the evolution predicted by the self-similar model. The dot-dashed line is the best fit to the unscaled high-redshift clusters (points not plotted) and can be used to judge the significance of the self-similar scaling.

the masses of the local systems were determined assuming isothermality, which enables a fair comparison with the high-redshift masses. Properties extrapolated to R_{200} were used, and a relation of the form

$$E(z)^{-7/3} \left(\frac{\Delta_v(z)}{\Delta_v(0)} \right)^{-7/6} L_{200(z)} = A \left(\frac{M_{200(z)}}{5 \times 10^{14} h_{70}^{-1} M_\odot} \right)^B$$

was fit to high- and low-redshift data separately.

Fig. 11 shows the best-fitting M – L relations for the two samples, and the parameters of the different relations are summarised in Table 6. The dot-dashed line shows the best-fitting M – L relation when no scaling for the predicted evolution is applied. The disagreement between that unscaled high- z relation and the local data is striking, even given the large scatter in the local data. However, when the high-redshift data are scaled by the predicted evolution, the best-fitting relation (solid line) agrees very well with the local relation (dashed line), with $\chi^2/\nu = 9.3/9$. The slopes of the low- and high- z relations are consistent, and are both steeper than the self-similar prediction of $4/3$ (although not very significantly for the high- z data). At least some of the larger scatter in the HIFLUGCS data is due to cooling cores in some systems, as no correction for these was made (Reiprich & Böhringer 2002).

10 DISCUSSION

The normalisation of the WARPS high-redshift scaling relations are all consistent with self-similar evolution of the local relations in a Λ CDM cosmology. We emphasise the importance of properly quantifying the effect of assuming

isothermality on the derived masses of high-redshift clusters when investigating the evolution of the M – T relations. The L – T and $M_{g,2500(z)}$ – T relations are the most robust of the high-redshift relations measured here, subject to the smallest systematic uncertainties and extrapolations. In particular the combined V02 and WARPS high- z sample enable the L – T relation to be measured with relatively small uncertainties. The M – L relation meanwhile is predicted to show the strongest evolution ($\propto E(z)^{-7/3} (\Delta_v(z)/\Delta_v(0))^{-7/6}$). The consistency of these relations with the predicted self-similar evolution provides strong evidence that that model is a good description of cluster evolution out to $z \approx 1$.

A preliminary measurement of the high-redshift $M_{2500(z)}$ – T relation in Maughan et al. (2003) found that it was consistent with no evolution, but did not strongly rule out self-similar evolution. This work improves on that earlier study in several ways. The sample used is larger, and the latest calibration was used in reanalysing the *Chandra* data (see §2). An important difference is that the masses are measured within radii corresponding to redshift-dependent density contrasts, estimated from the overdensity profile of each system. In the earlier study, the masses were measured within a fraction of the virial radius estimated from each cluster's temperature. The current study thus provides a more reliable measurement of the evolution of the $M_{2500(z)}$ – T relation.

The slope of the combined WARPS and V02 L – T relation is consistent with its low-redshift counterparts, and steeper than the slope of 2 predicted by the self-similar model. This suggests that the same processes are

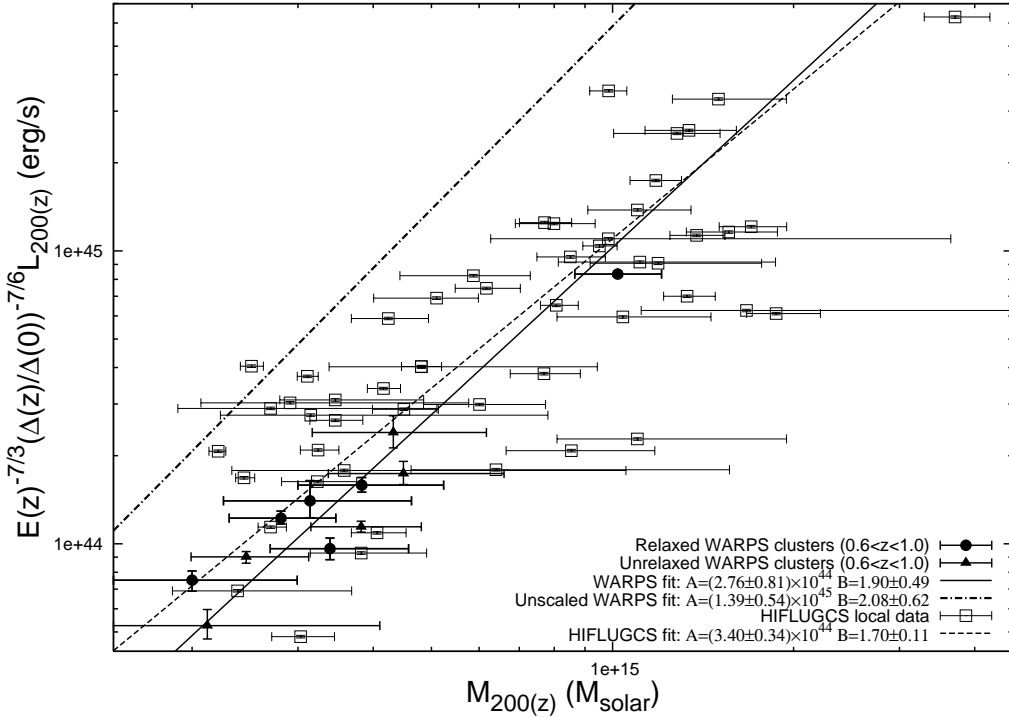


Figure 11. M – L relation for the low-z HIFLUGCS clusters and the high-z WARPS systems. Masses were measured within $R_{200(z)}$ assuming isothermality and luminosities within the same radius were scaled by the evolution predicted by the self-similar model. The dot-dashed line is the best fit to the unscaled high-redshift clusters (points not plotted) and can be used to judge the significance of the self-similar scaling.

M – L relation	$A (10^{44} h_{70}^{-2} \text{ erg s}^{-1})$	B	notes
Properties within $R_{200(z)}$			
WARPS M – L	2.76 ± 0.81	1.90 ± 0.49	$0.6 < z < 1.0$, luminosities scaled for predicted evolution (Fig. 11).
Unscaled WARPS M – L	13.8 ± 5.4	2.08 ± 0.62	$0.6 < z < 1.0$, no scaling for predicted evolution (Fig. 11).
HIFLUGCS M – L	3.40 ± 0.34	1.70 ± 0.11	Local clusters assuming isothermality (Fig. 11).

Table 6. Summary of the M – L relations discussed in §9.

responsible for the steepening of both relations, and non-gravitational processes have already influenced cluster properties by ($z \geq 1$). A possible interpretation of this is that the non-gravitational effects are important during the early stages of clusters' lives, regardless of redshift, as the clusters discussed here are generally relaxed in appearance, suggesting the major part of their formation is complete. The high-redshift M – L relation also supports this interpretation.

The slopes of $M_{200(z)} – T$ relation above 3 keV in both the WARPS and S03 samples are consistent with the self-similar prediction of 3/2. When the cooler S03 systems are included, the slope steepens, which is consistent with non-gravitational effects having a larger relative contribution in low-mass systems. Observations of cooler (< 3 keV) clusters at high-redshift are required to test whether there is any evolution in this effect. There is also a weak trend for the $M_{2500(z)} – T$ and $M_g 2500(z) – T$ relations to be steeper than the $M_{200(z)} – T$ and $M_g 200(z) – T$ relations, whose slopes agree more closely with the self-similar slope. This trend is present, though not strongly significant, in the high- and low-redshift relations. These results are consistent

with a scenario in which non-gravitational processes have a stronger effect in the central regions of clusters, which is more noticeable in cooler systems.

Generally, the M – T relations show a self-similar slope above 3 keV, the $M_g – T$ relations are self-similar, or slightly steeper, and the L – T relations are steeper than self-similar prediction. This suggests that although non-gravitational processes do not have a strong influence on the dark matter in > 3 keV clusters, those processes can still have an important effect on the gas in more massive systems.

10.1 Evolution of the L – T relation

As we saw in the §6, the evolution of the L – T relation is consistent with the self-similar model described in §4. The relatively large size of the combined WARPS and V02 samples also enables alternative models of cluster evolution that are used in the literature to be tested. As discussed in section §4, it is popular to use a fixed, redshift-independent density contrast to define the outer radius of clusters. In this case,

the L – T relation is given by

$$L_{\Delta}E(z)^{-1} \propto kT^B. \quad (16)$$

Now the $\Delta(z)^{-1/2}$ part of the normalisation is no longer required, and as this is an increasing function of z , the predicted L – T evolution is smaller than that predicted by the $\Delta(z)$ model. The measured luminosities are slightly larger when extrapolated to R_{Δ} instead of $R_{\Delta(z)}$, which acts in the opposite sense, increasing the apparent evolution. This evolution model was tested by comparing the combined WARPS and V02 L – T relation, with luminosities extrapolated to R_{200} (not $R_{200(z)}$) and scaled by $E(z)^{-1}$, with the local AE99 relation. The $E(z)^{-1}$ scaling was insufficient to reduce the luminosities to be consistent with the local L – T relation, with $\chi^2/\nu = 51/22$. This indicates that a redshift-dependent density contrast is required in the self-similar model to reconcile the high-redshift and local L – T relations.

A simple way of measuring the evolution of the L – T relation is to assume that it evolves as

$$L_{\Delta} \propto (1+z)^{\alpha} kT^B. \quad (17)$$

V02 found $\alpha = 1.5 \pm 0.3$ at 90% confidence by comparing their high-redshift data with the local Markevitch (1998) L – T relation. The combined WARPS and V02 L – T data were used to make a similar measurement. The luminosity of each cluster extrapolated to R_{200} was divided by $(1+z)^{\alpha}$, and the scaled data were compared with a local relation. This process was performed for a range of values of α , and for both of the local AE99 and Markevitch (1998) L – T relations and the results are shown in Fig. 12.

We find the best agreement between the scaled high-redshift data and the local AE99 relation, with $\alpha = 1.3 \pm 0.2$ (at the 90% level) and $\chi^2/\nu = 23.0/22$. Using the Markevitch (1998) relation as a low-redshift baseline results in a slightly lower value of α and a poorer fit. A measurement of α independent of that of V02 was also performed by using the WARPS sample alone. Compared with the AE99 local relation we find $\alpha = 0.8 \pm 0.4$ (90% level) while comparison with the Markevitch (1998) relation gives $\alpha = 0.7 \pm 0.4$ (90% level; see Fig. 13. These measurements are marginally consistent with the values of $\alpha = 1.5 \pm 0.3$ (68% level) found by Lumb et al. (2004) and 1.8 ± 0.3 (68% level) found by Kotov & Vikhlinin (2005) in samples of high-redshift clusters observed with *XMM-Newton*. We thus conclude that $\alpha \approx 1.2$ and that the range of values found is at least partially due to the uncertainty in the exact form of the local L – T relation.

While current the data cannot distinguish between a $L \propto (1+z)^{\alpha} kT^B$ model and the full self-similar $LE(z)^{-1} \Delta(z)^{-1/2} \propto kT^B$ model for the evolution of the L – T relation, the latter is more satisfactory because it is physically motivated, and does not introduce an additional free parameter (α).

Recent theoretical work has attempted to include the effects of preheating and radiative cooling in the simple self-similar scaling relations. Voit (2005) shows that introducing a cooling threshold $K_c = T^{2/3}t(z)^{2/3}$, where gas with an entropy less than K_c radiates all of its thermal energy away within a Hubble time $t(z)$, produces a “cooling threshold” L – T relation of the form

$$L \propto kT^{2.5} E(z)^{-1} t(z)^{-1}. \quad (18)$$

Voit (2005) also investigates the effect that including a modest initial amount of entropy in the gas before it is accreted onto a forming cluster has on the L – T relation. If the initial entropy level is chosen to match the observation that $K(0.1R_{200}) \propto kT^{2/3}$ (Ponman et al. 2003), then the resulting “altered similarity” L – T relation is

$$L \propto kT^3 E(z)^{-3} t(z)^{-2}. \quad (19)$$

Both of these modified self-similar models predict steeper L – T slopes which are in better agreement with observations than the simple self-similar slope of 2. The evolution of the L – T relation, however, is much milder in the modified self-similar models than in the simple self-similar model. Fig. 14 shows the evolution of the normalisation of the L – T relation for a variety of models. The data points show the observed evolution in the combined WARPS and V02 sample relative to the AE99 and Markevitch (1998) local relations. The data are binned by redshift, and the data points show the weighted mean and weighted standard deviation for each bin. While dividing the data into redshift bins may be pushing the limits of the current data, Fig. 14 serves to illustrate the range of predictions for the evolution of the L – T relation. The overall conclusion on the evolution of the L – T relation is that the self-similar model is a good description of the evolution out to $z \approx 1$. Larger samples at high redshifts will enable more detailed models to be tested, for example, indicating whether the evolution continues to increase with redshift, or flattens out in line with the predictions of the modified self-similar models.

10.2 Continuous formation predictions

The M – T relation defined in Equation 4 is derived under the late-formation approximation, in which a cluster forms in a single collapse, terminating with the system having just virialised at the redshift of observation. Several authors (e.g. Lacey & Cole 1993; Voit 2000) have derived M – T relations in a more realistic continuous-formation scenario, in which clusters grow by accumulating much smaller virialised objects. In a flat Λ CDM cosmology, Voit (2000) predicts

$$kT = (8.0 \text{ keV}) \left(\frac{M}{10^{15} h_{100}^{-1} M_{\odot}} \right)^{2/3} \frac{\xi_c(t)}{\xi_c(t_0)} \quad (20)$$

where $\xi_c(t)$ is the specific energy of a shell of matter which collapses onto the cluster at a time t (see the appendix of Voit 2000 for details). In this model, the evolution of the normalisation of the M – T relation is different from the late-formation predictions.

The continuous-formation model predicts that clusters of a given mass are cooler than the late-formation model predictions. However, the difference between the models is small at $z \approx 1$, requiring measurements of the M – T normalisation to a precision of $< 2\%$ to distinguish between them, and our results are consistent with either of these cluster-formation scenarios. The agreement between our measurements of the evolution of the M – T and M_g – T relations, and these models indicates that the properties of galaxy clusters reflect the properties of the universe at their redshift of observation. In the late-formation approximation this is simply because clusters formed at the redshift of observation, while in the continuous-formation model, the accretion

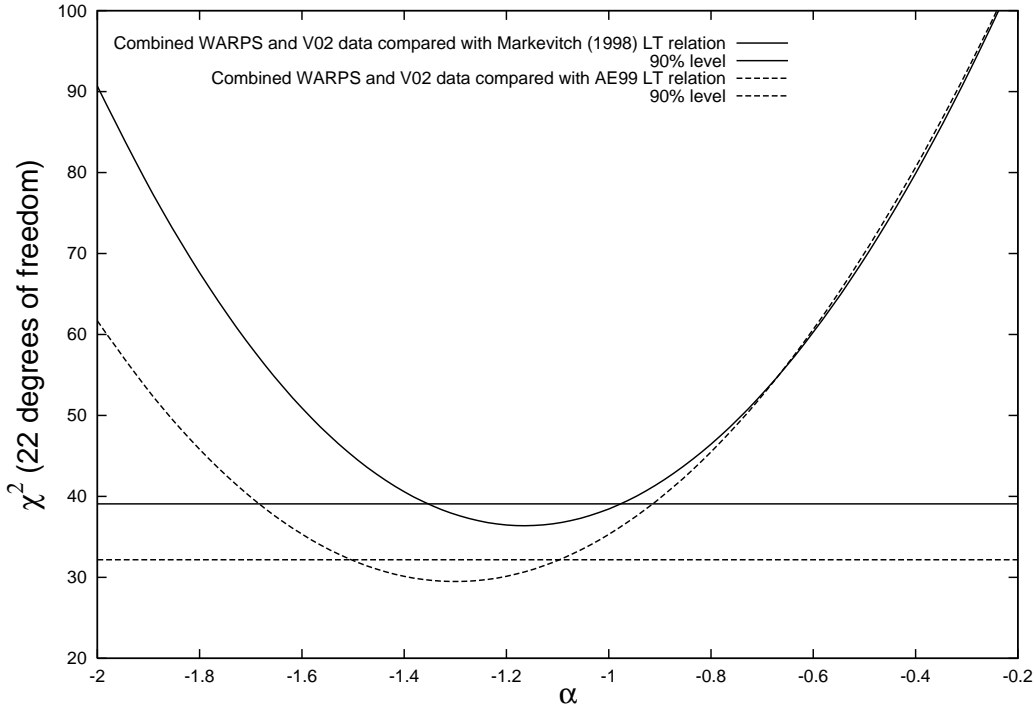


Figure 12. The χ^2 values for the comparison of the scaled high-redshift WARPS and V02 L – T data with the local relations. The luminosities of the high-redshift systems were scaled by $(1 + z)^{-\alpha}$ for different values of α .

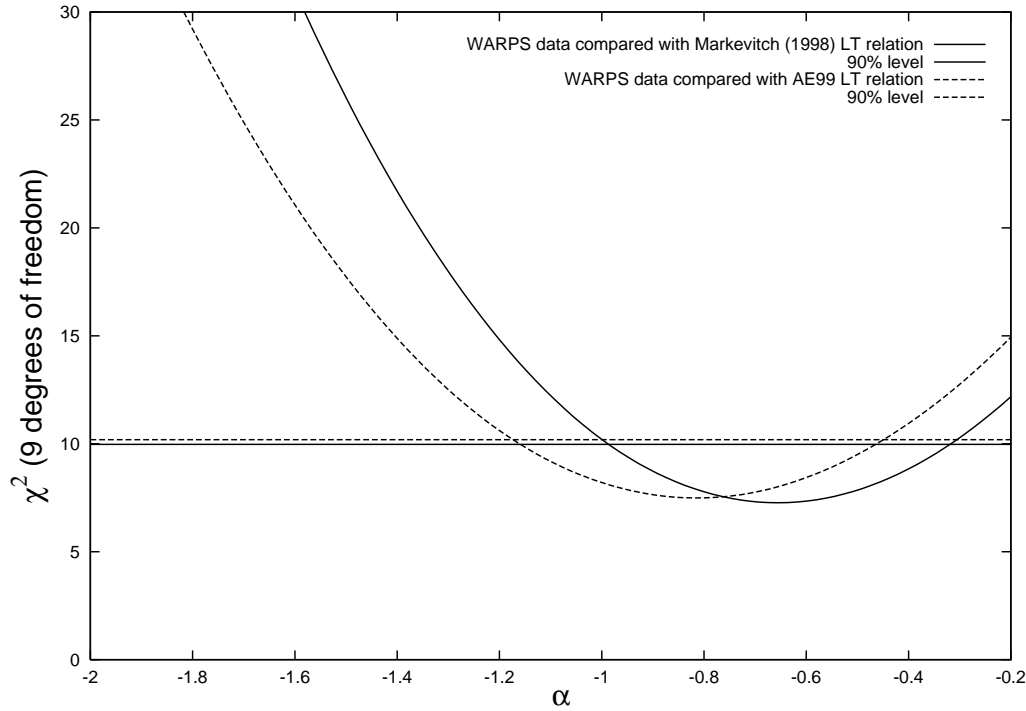


Figure 13. The χ^2 values for the comparison of the scaled high-redshift WARPS L – T data alone with the local relations. The luminosities of the high-redshift systems were scaled by $(1 + z)^{-\alpha}$ for different values of α .

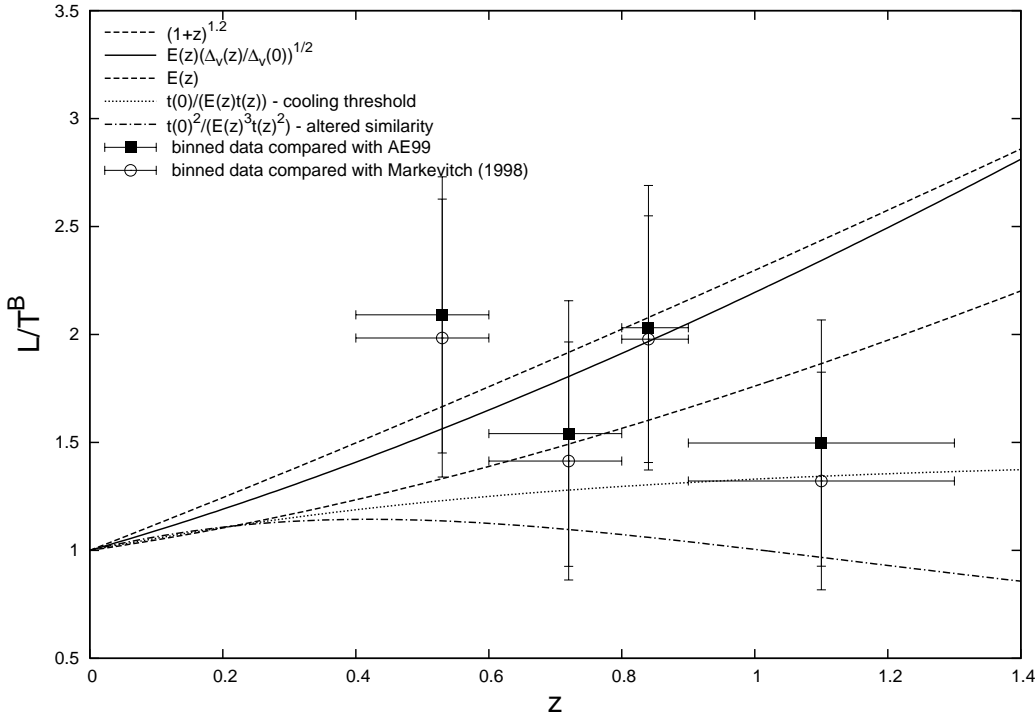


Figure 14. The evolution of the L – T relation normalisation predicted by different models. The data points are the observed evolution in the combined WARPS and V02 sample, in redshift bins, relative to different local L – T relation.

of matter onto clusters continually realigns their properties with those of the evolving universe.

10.3 Probing the redshift of virialisation

If clusters form in a single collapse, then they may virialise at a redshift (z_v) which is larger than their redshift of observation (z_{obs}). Their properties would then reflect those of the universe at an epoch earlier than z_{obs} , and the self-similar evolution which assumes $z_{\text{obs}} = z_v$ would not be a good description of the high-redshift scaling relations. If one is willing to assume that clusters obey self-similar evolution, then the high-redshift data can be used to place interesting constraints on the mean redshift of formation of the high-redshift sample (z_{vh}). If the mean redshift of formation of the local sample is denoted as z_{vl} , then the ratio of the normalisation of the low- and high-redshift L – T relations is given by $[E(z_{\text{vh}})\Delta_v(z_{\text{vh}})^{1/2}]/[E(z_{\text{vl}})\Delta_v(z_{\text{vl}})^{1/2}]$ (c.f. Equation 6).

Under the assumptions given above, the ratio of the normalisations of the high- and low-redshift L – T relations can be used to relate z_{vl} and z_{vh} . The high-redshift L – T relation thus allows z_{vh} to be measured for an assumed z_{vl} . A relation with a slope fixed at the local value of 2.88 (AE99) was fit to the unscaled WARPS and V02 high-z L – T data, and the best-fit normalisation, along with the maximum and minimum normalisations allowed by the data at the 99% level were found. These were then used to derive the constraints on z_{vh} plotted in Figure 15.

If the local or high-redshift clusters formed at a redshift other than z_{obs} , then the overdensity radii within which the luminosities are measured would be inappropriate. How-

ever, as the overdensity radii are all large and the surface-brightness is low in outer regions of the clusters, the use of different radii has a negligible effect. To illustrate this, if we consider a 6 keV cluster with $\beta = 0.67$ and $r_c = 100$ kpc observed at $z = 0$, we find $R_{200(z)} = 2.0$ Mpc for $z_v = 0$ and $R_{200(z)} = 1.6$ Mpc for $z_v = 1$. The luminosity of the cluster increases by just 1% between these two radii.

Figure 15 shows that if the local clusters are assumed to have virialised at $z = 0$, then the high-redshift data are consistent with $z_{\text{vh}} = z_{\text{obs}}$, with $z_{\text{vh}} < 1.5$ at the 99% level. We strongly rule out a common redshift of virialisation for the local and high-redshift samples, regardless of the redshift of formation of the local sample. That is not to say that the high-redshift clusters cannot evolve onto the local L – T relation, via mergers and accretion resetting their properties to new values of z_v . These results are simply indicating that the local clusters did not form fully at the same high redshift as the distant clusters and then evolve passively.

10.4 Properties of the WARPS clusters

The observed gas properties of the WARPS high-redshift sample are generally consistent with those of local clusters. The mean surface-brightness profile slope, $\bar{\beta} = 0.66 \pm 0.05$ is very close to the canonical value of 2/3 (Jones & Forman 1984). Also, the mean ratio of core radius to “virial radius” $r_c/R_{200(z)} = 0.14 \pm 0.05$ agrees well with the values found by Sanderson & Ponman (2003) for > 1 keV clusters. Furthermore, the gas-mass fractions found in the high-redshift clusters agree with those found in local clusters. The weighted mean f_{gas} at $R_{2500(z)}$ is 0.069 ± 0.012 , increasing to 0.11 ± 0.02 at $R_{200(z)}$ which agrees with the values found by S03. These

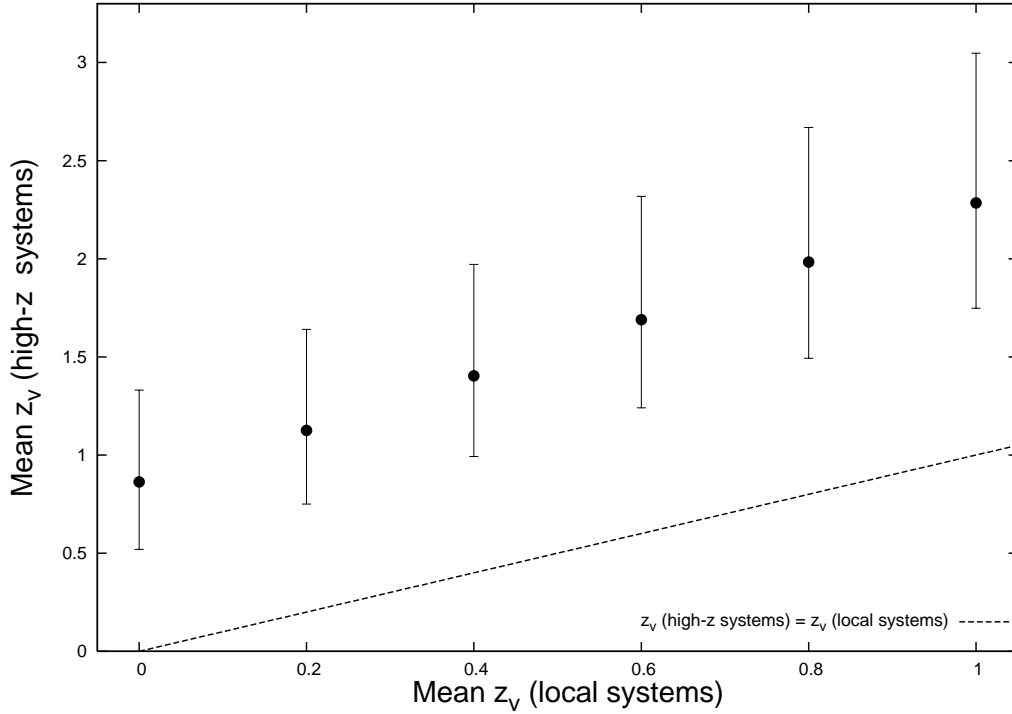


Figure 15. Constraints on the mean redshift of virialisation of the combined WARPS and V02 high-redshift sample derived from the evolution of the L – T relation. The dotted line indicates a common redshift of virialisation of the high- and low-redshift samples. Errorbars are 99%.

results indicate that the gas distribution is the same in low- and high-redshift clusters.

The metal abundances measured in the high-redshift systems are plotted against redshift in Fig. 16. The data (excluding ClJ1559.1+6353 with its very high, poorly constrained measurement) are consistent with the canonical value of $0.3Z_{\odot}$ out to $z = 1$; the weighted mean of the values is $0.28 \pm 0.11Z_{\odot}$. This is consistent with the high-redshift of enrichment of the intra-cluster medium found by other authors (e.g. Mushotzky & Loewenstein 1997; Tozzi et al. 2003).

11 CONCLUSIONS

The overall picture provided by this study of the evolution of the cluster scaling relations is that within the statistical limits of the current data, the evolution of galaxy clusters out to $z \approx 1$ is described well by the self-similar model. The large-scale properties of clusters are dominated by the density of the universe at the epoch at which they are observed.

12 ACKNOWLEDGEMENTS

We thank Alastair Sanderson for providing us with properties at different radii for the S03 sample. We are grateful to Stephen Helsdon for providing some of the software used for the regression line fitting. BJM was supported for the majority of this work by a Particle Physics and Astronomy Research Council (PPARC) postgraduate studentship. BJM

is currently supported by NASA through Chandra Postdoctoral Fellowship Award Number PF4-50034 issued by the Chandra X-ray Observatory Center, which is operated by the Smithsonian Astrophysical Observatory for and on behalf of NASA under contract NAS8-03060. HE gratefully acknowledges financial support from NASA grant NAG 5-10085.

REFERENCES

- Akritas M. G., Bershady M. A., 1996, ApJ, 470, 706
- Allen S. W., Schmidt R. W., Fabian A. C., 2002, MNRAS, 334, L11
- Arnaud M., Aghanim N., Neumann D. M., 2002, A&A, 389, 1
- Arnaud M., Evrard A. E., 1999, MNRAS, 305, 631
- Bower R. G., 1997, MNRAS, 288, 355
- Bryan G. L., Norman M. L., 1998, ApJ, 495, 80
- Cagnoni I., Elvis M., Kim D.-W., Mazzotta P., Huang J.-S., Celotti A., 2001, ApJ, 560, 86
- Cavaliere A., Fusco-Femiano R., 1976, A&A, 49, L137
- Dickey J. M., Lockman F. J., 1990, ARA&A, 28, 215
- Donahue M., Voit G. M., Scharf C. A., Gioia I. M., Mullis C. R., Hughes J. P., Stocke J. T., 1999, ApJ, 527, 525
- Ebeling H., Jones L. R., Perlman E., Scharf C., Horner D., Wegner G., Malkan M., Fairley B., Mullis C. R., 2000, ApJ, 534, 133
- Ebeling H., White D., Rangarajan F., 2005, MNRAS
- Ettori S., Tozzi P., Borgani S., Rosati P., 2004, A&A, 417, 13
- Fabian A. C., 1994, ARA&A, 32, 277

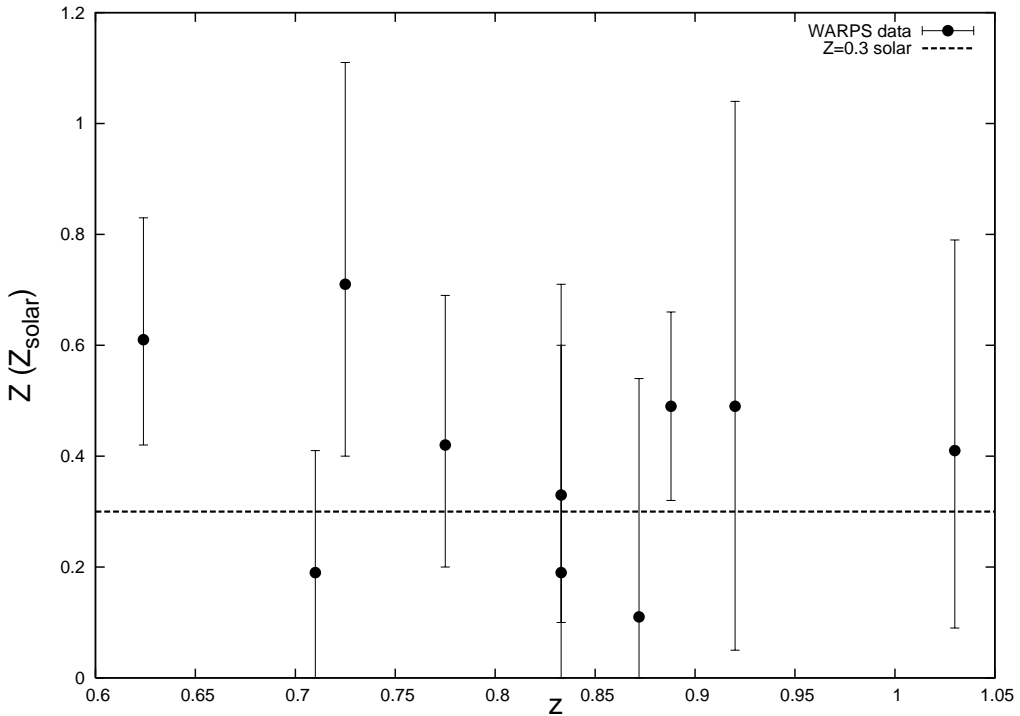


Figure 16. Cluster metallicity plotted against redshift for the WARPS high-redshift sample. Note that the poorly constrained high metallicity value measured in ClJ1559.1+6353 is not included in this plot.

Fairley B. W., Jones L. R., Scharf C., Ebeling H., Perlman E., Horner D., Wegner G., Malkan M., 2000, MNRAS, 315, 669

Huo Z., Xue S., Xu H., Squires G., Rosati P., 2004, AJ, 127, 1263

Jee M. J., White R. L., Benítez N., Ford H. C., Blakeslee J. P., Rosati P., Demarco R., Illingworth G. D., 2005, ApJ, 618, 46

Jones C., Forman W., 1984, ApJ, 276, 38

Kaastra J. S., Ferrigno C., Tamura T., Paerels F. B. S., Peterson J. R., Mittaz J. P. D., 2001, A&A, 365, L99

Kaastra J. S., Mewe R., 1993, A&AS, 97, 443

Kotov O., Vikhlinin A., 2005, ArXiv Astrophysics e-prints

Lacey C., Cole S., 1993, MNRAS, 262, 627

Lloyd-Davies E. J., Ponman T. J., Cannon D. B., 2000, MNRAS, 315, 689

Lumb D. H., Bartlett J. G., Romer A. K., Blanchard A., Burke D. J., Collins C. A., Nichol R. C., Giard M., Marty P. B., Nevalainen J., Sadat R., Vauclair S. C., 2004, A&A, 420, 853

Markevitch M., 1998, ApJ, 504, 27

Maughan B. J., Jones L. R., Ebeling H., Perlman E., Rosati P., Frye C., Mullis C. R., 2003, ApJ, 587, 589

Maughan B. J., Jones L. R., Ebeling H., Scharf C., 2004, MNRAS, 351, 1193

Maughan B. J., Jones L. R., Lumb D., Ebeling H., Gondoin P., 2004, MNRAS, 354, 1

Mushotzky R. F., Loewenstein M., 1997, ApJ, 481, L63

Mushotzky R. F., Scharf C. A., 1997, ApJ, 482, L13

Perlman E. S., Horner D. J., Jones L. R., Scharf C. A., Ebeling H., Wegner G., Malkan M., 2002, ApJS, 140, 265

Ponman T. J., Cannon D. B., Navarro J. F., 1999, Nature, 397, 135

Ponman T. J., Sanderson A. J. R., Finoguenov A., 2003, MNRAS, 343, 331

Reiprich T. H., Böhringer H., 2002, ApJ, 567, 716

Sanderson A. J. R., Finoguenov A., Mohr J. J., 2004, ArXiv Astrophysics e-prints

Sanderson A. J. R., Ponman T. J., 2003, MNRAS, 345, 1241

Sanderson A. J. R., Ponman T. J., Finoguenov A., Lloyd-Davies E. J., Markevitch M., 2003, MNRAS, 340, 989

Scharf C., Jones L. R., Ebeling H., Perlman E., Malkan M., Wegner G., 1997, ApJ, 477, 79

Tozzi P., Rosati P., Ettori S., Borgani S., Mainieri V., Norman C., 2003, ApJ, 593, 705

Vikhlinin A., Kravtsov A., Forman W., Jones C., Markevitch M., Murray S. S., Van Speybroeck L., 2005, ArXiv Astrophysics e-prints

Vikhlinin A., VanSpeybroeck L., Markevitch M., Forman W. R., Grego L., 2002, ApJ, 578, L107

Voit G. M., 2000, ApJ, 543, 113

Voit G. M., 2005, Reviews of Modern Physics, 58, 1